ATHEROSCLEROSIS

Noncanonical inhibition of caspase-3 by a nuclear microRNA confers endothelial protection by autophagy in atherosclerosis

Donato Santovito[1,2]*†, Virginia Egea[1]*, Kiril Bidzhekov[1]*, Lucia Natarelli[1,2]*, André Mourão[3], Xavier Blanchet[1], Kanin Wichapong[4], Maria Aslani[1,2], Coy Brunßen[5], Michael Horckmans[1,6], Michael Hristov[1], Arie Geerlof[3], Esther Lutgens[1,2,7], Mat J.A.P. Daemen[7], Tilman Hackeng[4], Christian Ries[1], Triantafyllos Chavakis[8], Henning Morawietz[5], Ronald Naumann[9], Philipp von Hundelshausen[1,2], Sabine Steffens[1,2], Johan Duchêne[1], Remco T.A. Megens[1,4], Michael Sattler[3,10], Christian Weber[1,2,4,11]†

MicroRNAs (miRNAs) are versatile regulators of gene expression with profound implications for human disease including atherosclerosis, but whether they can exert posttranslational functions to control cell adaptation and whether such noncanonical features harbor pathophysiological relevance is unknown. Here, we show that miR-126-5p sustains endothelial integrity in the context of high shear stress and autophagy. Bound to argonaute-2 (Ago2), miR-126-5p forms a complex with Mex3a, which occurs on the surface of autophagic vesicles and guides its transport into the nucleus. Mutational studies and biophysical measurements demonstrate that Mex3a binds to the central U- and G-rich regions of miR-126-5p with nanomolar affinity via its two K homology domains. In the nucleus, miR-126-5p dissociates from Ago2 and binds to caspase-3 in an aptamer-like fashion with its seed sequence, preventing dimerization of the caspase and inhibiting its activity to limit apoptosis. The antiapoptotic effect of miR-126-5p outside of the RNA-induced silencing complex is important for endothelial integrity under conditions of high shear stress promoting autophagy: ablation of Mex3a or ATG5 in vivo attenuates nuclear import of miR-126-5p, aggravates endothelial apoptosis, and exacerbates atherosclerosis. In human plaques, we found reduced nuclear miR-126-5p and active caspase-3 in areas of disturbed flow. The direct inhibition of caspase-3 by nuclear miR-126-5p reveals a noncanonical mechanism by which miRNAs can modulate protein function.

INTRODUCTION

Beyond shaping gene expression by guiding argonaute (AGO) proteins to target RNA transcripts in the RNA-induced silencing complex (RISC), it remains unclear whether microRNAs (miRNAs) can also regulate cell functions by additional mechanisms. To exert their posttranscriptional activity, miRNAs require multiple components such as trinucleotide repeat containing adaptor 6A (TNRC6A) in high-molecular weight RISCs to allow for interaction of the miRNA with the 3′ untranslated region of target mRNAs and with enzymes mediating inhibition of translation or RNA decay (*1*, *2*). Beyond such prototypic effects, miRNAs can be retained in low-molecular weight (LMW) complexes with AGO2 not bound to mRNA or engaged in target repression. Although viewed as a miRNA reservoir, it is unknown and debatable whether these complexes may enable interactions of hosted miRNAs with proteins not involved in the canonic functions of the RISC, whether these miRNAs can thereby exert direct posttranslational effects on protein activities, and how this is related to their intracellular trafficking.

Assembly of LMW complexes is controlled by mammalian target of rapamycin (mTOR) complex I and prevails upon mTOR inhibition (*3*–*5*). Inhibition of mTOR is one of the most powerful triggers of autophagy, a catabolic process used by eukaryotic cells for adapting to stress, for maintaining nutrient homeostasis, and for mediating quality control and lysosomal degradation of damaged organelles and protein aggregates (*6*, *7*). In endothelial cells (ECs), autophagic flux is triggered via the mTOR pathway by high shear stress (HSS) and is impaired at predilection areas for atherosclerosis (*8*), but the mechanisms by which laminar shear stress and autophagy regulate miRNA fate and function in this context are poorly understood.

The Krüppel-like family of transcription factors (KLFs) is an important regulator of autophagy, which has emerged as a rheostat of the miRNA-processing machinery to control mature miRNA expression (*9*–*12*). KLF2 coordinates most of the transcriptional programs evoked by shear stress in arterial ECs and is required for blood flow–dependent miR-126 expression in zebrafish (*12*–*15*). Among the most highly expressed endothelial miRNAs, the miR-126 duplex is instrumental for angiogenesis and vascular integrity, featuring strand-specific functions and homeostasis (*16*–*19*). Whereas miR-126-3p mediates

[1]Institute for Cardiovascular Prevention (IPEK), Ludwig-Maximillians-Universität (LMU) München, D-80336 Munich, Germany. [2]German Center for Cardiovascular Research (DZHK), partner site Munich Heart Alliance, D-80336 Munich, Germany. [3]Institute of Structural Biolology, Helmholtz Zentrum München, D-85764 Neuherberg, Germany. [4]Department of Biochemistry, Cardiovascular Research Institute Maastricht (CARIM), Maastricht University, 6229HX Maastricht, Netherlands. [5]Division of Vascular Endothelium and Microcirculation, Department of Medicine III, Faculty of Medicine, TU Dresden, D-01307 Dresden, Germany. [6]Institut de Recherche Interdisciplinaire en Biologie Humaine et Moléculaire, Université Libre de Bruxelles (ULB), B-1070 Brussels, Belgium. [7]Department of Medical Biochemistry and Pathology, Amsterdam University Medical Centers, Amsterdam School of Cardiovascular Sciences (ACS), 1081HZ Amsterdam, Netherlands. [8]Institute of Clinical Chemistry and Laboratory Medicine, Faculty of Medicine, TU Dresden, D-01307 Dresden, Germany. [9]Max-Planck-Institute of Molecular Cell Biology and Genetics, D-01307 Dresden, Germany. [10]Center for Integrated Protein Science Munich at Biomolecular NMR Spectroscopy, Department of Chemistry, Technical University of Munich, D-85747 Garching, Germany. [11]Munich Cluster for Systems Neurology (SyNergy), D-81377 Munich, Germany.
*These authors contributed equally to this work.
†Corresponding author. Email: chweber@med.lmu.de (C.W.); donato.santovito@gmail.com (D.S.)

proangiogenic and anti-inflammatory signaling, miR-126-5p maintains the EC proliferative reserve, modulating distinct targets and pathways (*16*, *17*, *19*–*22*). In line with differential functions, only miR-126-5p is up-regulated by laminar flow in arterial ECs to limit atherosclerosis in areas of HSS (*16*). Although both strands are processed from a common precursor by the endoribonuclease Dicer, their arterial quantities are not affected by EC-specific Dicer deletion (*23*). Thus, the differential regulation of miR-126 strands does not rely on transcription or processing, leaving underlying mechanisms such as shear stress–elicited autophagy to be elucidated. In the current study, we sought to detail the role of EC autophagy in the strand-specific regulation and intracellular trafficking of miR-126 upon HSS and specifically identified a function of the RNA binding protein Mex3a in the nuclear enrichment of miR-126-5p. Moreover, we found a noncanonical mechanism of action for nuclear miR-126-5p by demonstrating its ability to inhibit caspase-3 activity by direct miRNA-protein interaction. In concert, our findings unveil a crucial pathway for sustaining endothelial integrity by limiting apoptotic EC death.

RESULTS

HSS and autophagy promote nuclear miR-126-5p enrichment

To better understand the interplay of laminar shear stress and autophagy in controlling the expression of miRNAs, namely, miR-126, we overexpressed KLF2 in human umbilical vein ECs (HUVECs), showing increased pre–miR-126 and miR-126-5p but not miR-126-3p expression (Fig. 1A and fig. S1, A to C). Accordingly, we detected lower amounts of miR-126-5p but not miR-126-3p in the aortic intima of $Cdh5^{Cre}Klf2^{fl/fl}$ mice with EC-specific *Klf2* deletion (Fig. 1B), thus implicating mechanisms of posttranscriptional strand regulation. KLF2 overexpression and HSS (12 dyne/cm^2) increased autophagy-related gene (ATG) transcripts and promoted autophagic flux, as indicated by the conversion of microtubule-associated protein-1 light chain 3 (LC3)–I to autophagosome-associated LC3-II and by the reduction of the autophagy substrate p62 at the protein but not at the transcript level (Fig. 1, C and D, and fig. S1, D to H). We next scrutinized whether autophagy is involved in the differential regulation of miR-126 strands. Eliciting autophagy with the mTOR inhibitor rapamycin in ECs reduced the amount of miR-126-3p, whereas that of miR-126-5p was preserved (Fig. 1E and fig. S2, A to C). This was not due to extracellular release, because shedding and miR-126-3p content of apoptotic bodies (ABs) were attenuated (fig. S2, D to F) but was rather due to autophagy-related degradation activity, as shown by silencing of ATG5 or ATG7 or by blocking autophagosome/lysosome fusion with bafilomycin, which restored miR-126-3p amounts (Fig. 1E).

Localization to subcellular compartments is pivotal to miRNA function (*2*, *3*); therefore, we probed whether this segregation also regulates miR-126 expression. Transfecting fluorescently tagged mimics revealed a prominent nuclear localization enhanced by rapamycin for miR-126-5p but not for miR-126-3p (Fig. 1, F to H). Fractional quantitative polymerase chain reaction (qPCR) confirmed rapamycin-induced nuclear enrichment of endogenous miR-126-5p (Fig. 1I and fig. S2, G and H). Silencing of ATG5 and ATG7 or using the α/β-importin inhibitor ivermectin prevented nuclear miR-126-5p accumulation (Fig. 1J). Limiting autophagy by 3-methyladenine blunted the KLF2-driven increase in nuclear miR-126-5p (Fig. 1K). Likewise, exposure of ECs to physiological laminar shear stress (12 dyne/cm^2) (*24*) revealed a nuclear enrichment of miR-126-5p when compared to static conditions, exposure to low shear stress (LSS; 1 dyne/cm^2), or to shear stress exceeding the physiological range (30 dyne/cm^2) (fig. S2I). Together, autophagic flux triggered by KLF2 or mTOR inhibition governs trafficking of miR-126 strands, preserving miR-126-5p by nuclear transfer.

Studies using compartment-specific microinjection found that synthetic miR-21 and let-7a shuttle between nucleus and cytoplasm (*25*); however, we did not detect effects of rapamycin on nuclear amounts of let-7a-3p/let-7a-5p, miR-21-3p/miR-21-5p nor the miR-17 duplex with two functional strands (*26*) (Fig. 2A). Hence, autophagy-driven nuclear enrichment is not a general mechanism pertaining to all miRNA strands but preferentially affects miR-126-5p, although it lacks the hexanucleotide AGUGUU motif known to facilitate nuclear enrichment (*27*). Availability or subcellular distribution of strand-specific target transcripts, which can influence nuclear shuttling (*25*), was unaltered by rapamycin or KLF2 overexpression (fig. S2, J to L). To explore sequence determinants for nuclear translocation, we assessed mutational changes in fluorescent synthetic miR-126-5p. Whereas the seed sequence required for canonical binding of RNA targets (*2*) was dispensable for rapamycin-promoted nuclear shuttling (Mut1 and Mut2), more extensive mutation of nucleotides spanning to the 3′ end (Mut3) abrogated nuclear enrichment (Fig. 2, B to D). Thus, the specificity of nuclear miR-126-5p translocation does not rely on its seed sequence or seed-matched transcripts but requires other sequence motifs.

Nuclear translocation of miR-126-5p requires the RNA binding protein Mex3a

Stabilization by AGO proteins contributes to the nuclear persistence of shuttled miRNAs, and AGO2 is capable of shuttling and indispensable for unwinding and strand selection (*3*, *25*, *28*). Although the overall amount of AGO2 was unaltered (fig. S3A), we found that rapamycin elicited nuclear accumulation of AGO2 and LC3, which was blocked by ivermectin (Fig. 3A and fig. S3B). RNA-immunoprecipitation (IP) verified preferential binding of miR-126-5p to nuclear AGO2 (Fig. 3B). At the nanoscopic level, AGO2 was detectable on the outer surface rather than in the lumen of LC3-demarcated vesicles in rapamycin-treated ECs (Fig. 3C). Moreover, we isolated autophagosomes by density-gradient centrifugation to use a protease protection assay, on the basis of the principle that components included inside the autophagosome will resist digestion by proteases (*29*). Incubation of isolated autophagosomes with trypsin dose-dependently decreased the amount of AGO2 but not that of LC3-II (which is also bound to the intraluminal membrane), thus further supporting the localization of AGO2 on the extraluminal surface (fig. S3C). This complies with evidence that AGO2 binds to intracellular membranes, including those likely involved in phagophore elongation (*30*), and could explain why AGO2:miR-126-5p complexes are preserved from degradation. Together, our data support the concept that sorting of AGO2:miR-126-5p complexes on autophagosomal surfaces promotes nuclear translocation.

How does autophagy drive nuclear enrichment? In T cells, mTOR controls the assembly of LMW miRNA:AGO2 complexes, which represent a cellular miRNA reservoir and the prevalent nuclear form (*3*–*5*, *31*). Size exclusion chromatography in ECs revealed that mTOR inhibition shifted AGO2 coelution toward LMW complexes, which prevail in nuclear fractions and were devoid of the RISC protein TNRC6A (fig. S3, D and E), implying that autophagy shapes AGO2

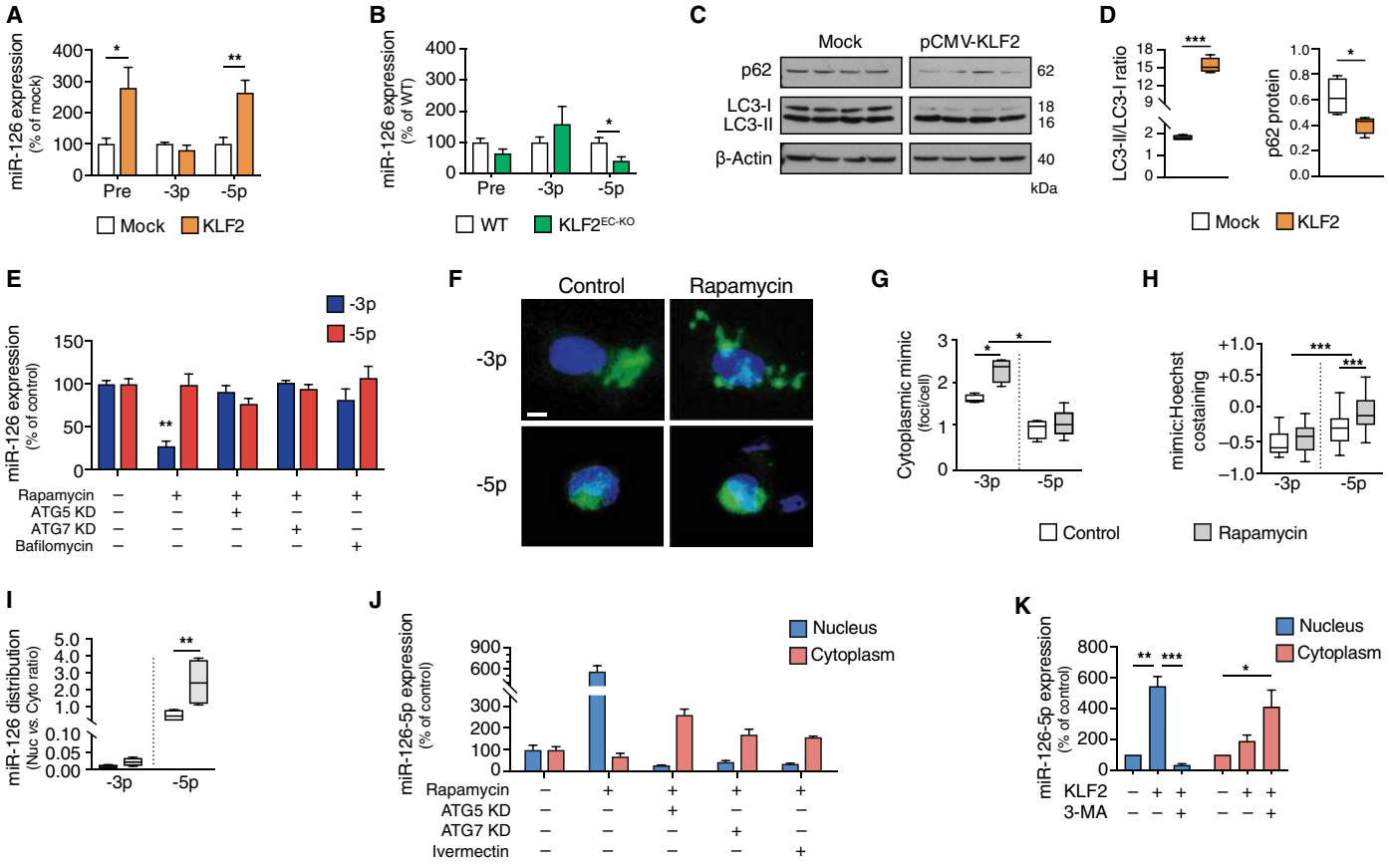

Fig. 1. KLF2-induced autophagy triggers differential regulation of miR-126 strands and miR-126-5p nuclear localization. (**A**) Expression of pre–miR-126, miR-126-3p, and miR-126-5p in HUVECs overexpressing KLF2 ($n = 5$ to 7) and (**B**) in aortic intima of *Cdh5*^{Cre}*Klf2*$^{fl/fl}$ (KLF2$^{EC\text{-}KO}$) and control mice [wild type (WT)] ($n = 4$ to 5). (**C**) Western blot analysis of autophagy markers upon KLF2 overexpression and (**D**) densitometric quantification of the LC3-II/LC3-I ratio and p62 expression (normalized to β-actin) ($n = 4$). (**E**) Amounts of miR-126-3p and miR-126-5p in HUVECs treated with rapamycin and bafilomycin ($n = 6$). KD, knockdown. (**F**) Representative immunofluorescence of miR-126-3p and miR-126-5p mimics (green) in HUVECs treated with or without rapamycin. Scale bar, 5 μm. (**G**) Quantification of cytoplasmic mimic foci per cell ($n = 4$ to 5) and (**H**) Pearson's colocalization coefficient for mimic and Hoechst nuclear dye ($n = 39$ to 69 cells). (**I**) Nucleocytoplasmic distribution of endogenous miR-126 strands in HUVECs upon rapamycin treatment ($n = 4$). (**J**) Nuclear (Nuc) and cytoplasmic (Cyto) amounts of miR-126-5p in HUVECs treated with rapamycin and silencing of autophagy rate-limiting proteins (ATG5 or ATG7) or cotreated with the importin inhibitor ivermectin ($n = 3$ to 6) and (**K**) in HUVECs overexpressing KLF2 treated with the autophagy inhibitor 3-methyladenine (3-MA) ($n = 3$). $^*P < 0.05$, $^{**}P < 0.01$, $^{***}P < 0.001$. Two-tailed Student's *t* test (A, B, and D) or factorial ANOVA with Bonferroni post hoc test (E, G to I, and K).

interactions by degrading RISC components to favor nuclear transfer. Hence, we performed AGO2-IP to identify interacting proteins. Despite the contiguity observed (Fig. 3, A and C), LC3 was not detected in AGO2 immunoprecipitates of rapamycin-treated cells nor were the nuclear AGO2 navigators TNRC6A and importin-8 (Fig. 3D) (*32*–*34*), thus excluding their involvement. Among AGO2-interacting proteins capable of nuclear-cytoplasmic shuttling, Mex3a, a member of the RNA binding Mex3 family, forms RNA-mediated bonds in P-bodies (*35*, *36*). Co-IP revealed interactions of AGO2 and Mex3a in both cytoplasm and nuclei, and this was validated by confocal microscopy of autophagic ECs (Fig. 3, D and E). Mex3a was degraded by trypsin in the autophagosome protection assay and coeluted with AGO2 in LMW complexes, suggesting that it localizes on the outer autophagosome membrane to mark and facilitate AGO2 complexes suited for nuclear translocation (fig. S3, C to E). Conversely, we failed to detect interactions with Mex3c or the P-body core-protein decapping protein 1a (DCP1a), indicating a role for Mex3a unrelated to P-bodies (Fig. 3D). Using stimulated emission depletion (STED) nanoscopy to detail this complex confirmed colocalizing signals for AGO2 and Mex3a, whereas LC3 signals showed only proximity (Fig. 3F). In addition, rapamycin reduced cytoplasmic Mex3a, increasing its nuclear localization in the vicinity of LC3 (fig. S3, F to I).

Mex3a preferentially binds to miR-126-5p

We next characterized RNA binding of Mex3a, which is imparted by two K homology (KH) domains (*35*). Nuclear magnetic resonance (NMR) titrations indicated that the heterogeneous tandem KH domains bind to miR-126-5p consistent with submicromolar affinity (Fig. 4A). Surface plasmon resonance (SPR) confirmed high-affinity binding of full-length Mex3a to immobilized miR-126-5p (Fig. 4B). To verify how structural accommodation of miR-126-5p binding by both KH domains can occur, we performed small-angle x-ray scattering (SAXS) to show that the free KH1 and KH2 tandem domains are flexibly connected, resembling pearls on a string, whereas they form a compact arrangement when bound to miR-126-5p (Fig. 4C and fig. S4A). Next, we computed homology models based on the

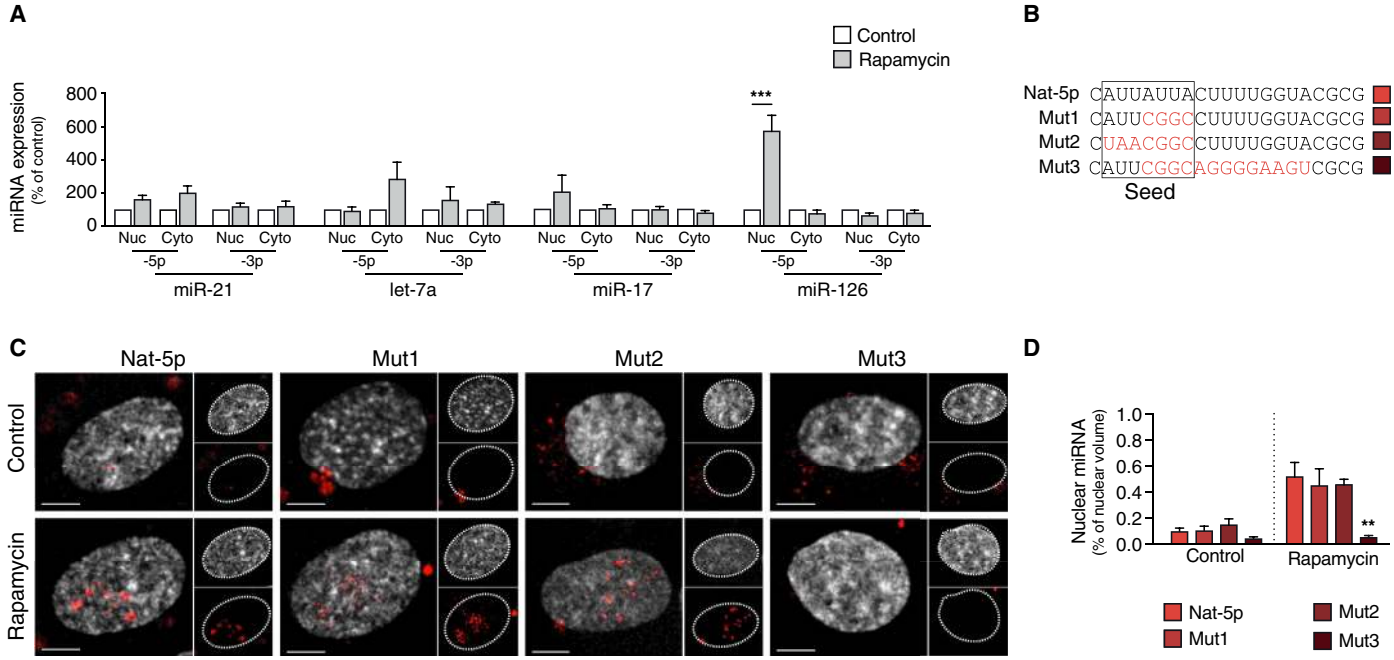

Fig. 2. Preferential nuclear transfer of miR-126-5p is unrelated to its seed sequence. (**A**) Nuclear and cytoplasmic amounts of both strands of miR-21, let-7a, miR-17, and miR-126 in HUVECs treated with or without rapamycin, as assessed by qPCR ($n = 3$ to 4). (**B**) Sequences of miR-126-5p and mutants (Mut1 to Mut3) transfected in HUVECs. (**C**) Confocal microscopy showing localization of miR-126-5p (Nat-5p) and mutants (Mut1 to Mut3, red) in 4′,6-diamidino-2-phenylindole (DAPI)–stained nuclei (gray). (**D**) Quantification of mean nuclear volume occupied by mutants assessed after 3D deconvolution and rendering ($n = 4$ to 6). Scale bars, 5 μm. $^{**}P < 0.01$ and $^{***}P < 0.001$. Factorial ANOVA with Bonferroni post hoc test (A and D).

cocrystal structures of individual Mex3c KH domains with RNA (fig. S4, B to D) (*37*). These models imply a mode of interaction in which the two KH domains recognize nucleotides U_3-U_6 and G_{15}-C_{18} in miR-126-5p. Estimated binding free energies (BFEs) indicated preferential binding of the 5p versus 3p strand (Fig. 4D and fig. S4, E to G), which was consistent with reduced spectral changes in NMR titrations (fig. S5A). Preferential binding of miR-126-5p was experimentally confirmed by SPR on immobilized Mex3a, by isothermal titration calorimetry (ITC), and by pulldown of biotinylated miR-126 strands after exposure to nuclear lysates (Fig. 4D and fig. S5, B to F). Consistently, RNA-IP of nuclear Mex3a in rapamycin-treated ECs unveiled a preferential enrichment of miR-126-5p (Fig. 4E). SPR revealed that AGO2:Mex3a interactions only occur in the presence of miR-126-5p, either immobilized or in solution, indicating privileged binding by ternary interactions in a complex (Fig. 4, F and G, and fig. S5, G and H). In the nucleus, the presence of a ternary complex was visualized by fluorescence in situ hybridization (FISH) for miR-126-5p and coimmunostaining for Mex3a and AGO2 (fig. S5I). Last, silencing Mex3a abrogated the rapamycin-induced AGO2 and LC3 accumulation (Fig. 4H and fig. S3I) and miR-126-5p enrichment in EC nuclei (Fig. 4I). Together, our findings establish that nuclear shuttling of a miR-126-5p:AGO2 complex is mediated by a Mex3a-dependent process.

Nuclear miR-126-5p exerts antiapoptotic properties

Nuclear AGO2:miRNA complexes have been described to affect the transcriptome via diverse mechanisms (*3*, *25*, *33*, *38*). Hence, we assessed transcriptional effects of nuclear miR-126-5p transfer by evaluating changes in gene expression after short-term exposure to rapamycin combined with gain- and loss-of-function for miR-126-5p. Expression of multiple transcripts involved in EC biology was altered, and we analyzed the functional annotation for those undergoing concordant regulation with both rapamycin and miR-126-5p mimics (Fig. 5A). Because the analysis of the Kyoto Encyclopedia of Genes and Genomes (KEGG) pathway enrichment revealed predominant effects on transcriptional profiles of apoptosis-related pathways (Fig. 5B), we assessed apoptosis mediators at the protein level. Overexpression of miR-126-5p only slightly attenuated caspase-3/9 expression but markedly reduced the active form of caspase-3 and cleavage of its substrates, an effect which required the presence of rapamycin to induce nuclear transfer of miR-126-5p, and was not observed upon miR-126-5p inhibition (Fig. 5C). Conversely, impeding nuclear enrichment of miR-126-5p by Mex3a knockdown increased caspase-3 cleavage (Fig. 5D). A reduction in EC apoptosis after rapamycin treatment was prevented by silencing miR-126-5p or Mex3a (Fig. 5, E and F). Likewise, antiapoptotic effects mediated by Mex3a overexpression were impaired by miR-126-5p silencing (Fig. 5G).

Direct interaction with caspase-3 conveys antiapoptotic effects of miR-126-5p

Antiapoptotic effects occurred rapidly upon treatment with rapamycin and preceded transcriptional changes in relevant mediators (fig. S6A), leading us to postulate direct antiapoptotic properties of miR-126-5p. As an effector caspase, caspase-3 acts downstream in the apoptotic cell death cascade and can translocate to the nucleus after proteolytic activation and substrate recognition (*39*). Therefore, we tested potential interactions with the miR-126-5p complex. Applying a support vector machine classifier based on sequences of caspase-3 and miR-126-5p (RPISeq-SVM), we derived a probability of interaction, which was higher than miR-126-3p (fig. S6B). Similarly, molecular dynamics simulation (MDS) supported a preferential binding of miR-126-5p compared to other abundant endothelial miRNAs

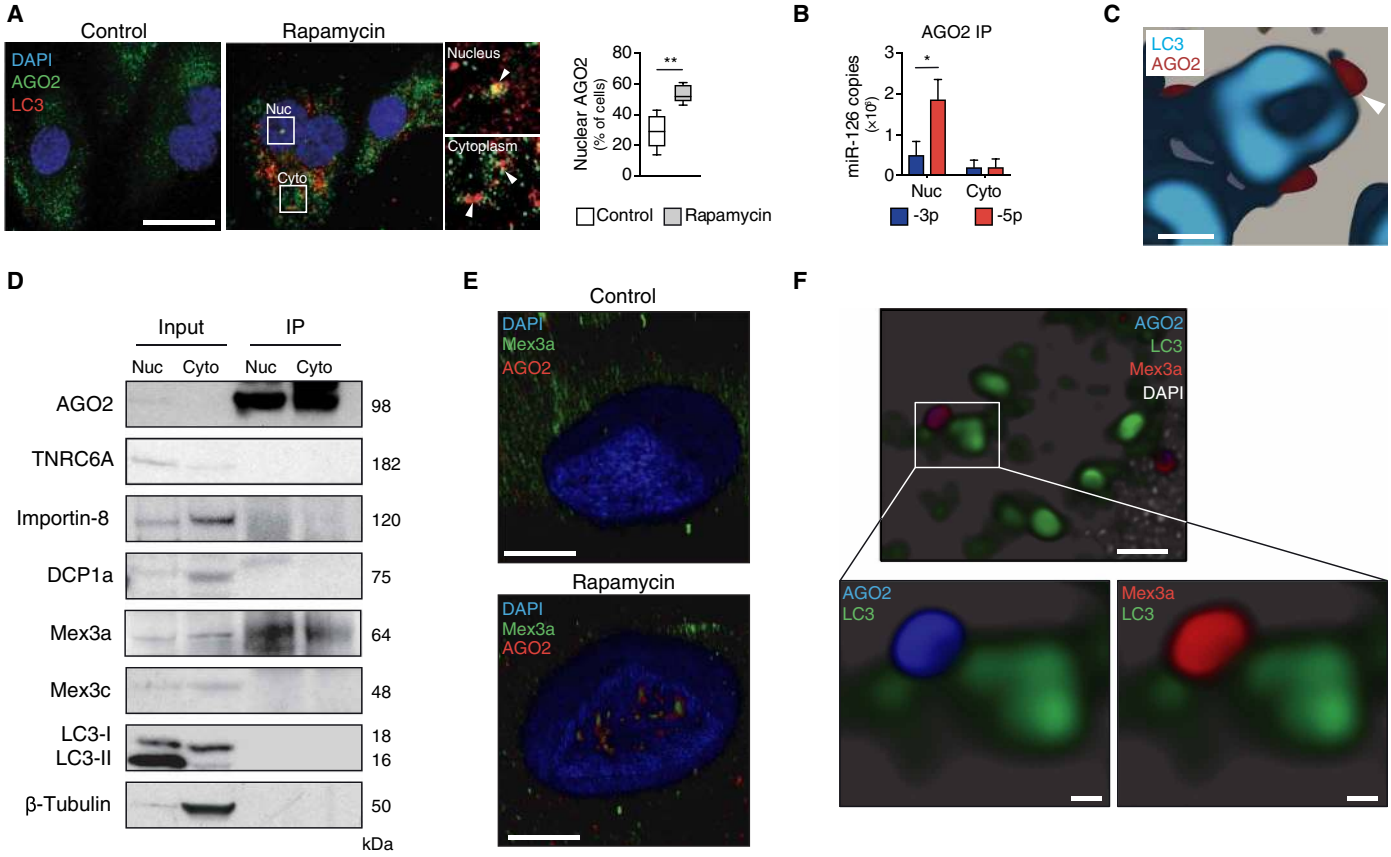

Fig. 3. Nuclear miR-126-5p interacts with the RNA binding protein Mex3a and AGO2. (**A**) Immunofluorescence for AGO2 and LC3 in rapamycin-treated HUVECs and controls and quantification of nuclear AGO2-positive cells. Insets show colocalizing signals (white arrowheads) ($n = 5$). Scale bar, 20 μm. (**B**) RNA-IP of nuclear and cytoplasmic AGO2 in rapamycin-treated HUVECs showing miR-126 strand loading. (**C**) STED nanoscopy showing AGO2 signals on the outer surface of a LC3-demarcated vesicle (white arrowhead). Scale bar, 200 nm. (**D**) Co-IP of AGO2 and Mex3a in rapamycin-treated HUVECs. (**E**) 3D confocal microscopy for AGO2 and Mex3a in the nucleus of rapamycin-treated HUVECs and controls. Scale bars, 5 μm. (**F**) STED nanoscopy detailing the AGO2:Mex3a:LC3 cytoplasmic complex in rapamycin-treated HUVECs. Scale bar, 1 μm (top). Magnification of the complex is shown for the two fluorescent channels (AGO2 with LC3 and Mex3a with LC3) in the bottom panels. Scale bars, 200 nm. *$P < 0.05$ and **$P < 0.01$. Two-tailed Student's *t* test (A) and two-factor repeated measures ANOVA with Bonferroni post hoc test (B).

(table S1). Experimentally, FISH acquired by confocal microscopy showed colocalizing signals for miR-126-5p and caspase-3, particularly in nuclear and perinuclear areas, and this colocalization was reduced by Mex3a knockdown (Fig. 6, A to C). RNA-IP demonstrated a marked enrichment of miR-126-5p (but not other miRNAs) associated with nuclear caspase-3 upon rapamycin treatment or under conditions of HSS (Fig. 6D and fig. S6C). Although no interaction of caspase-3 and AGO2 was detectable in co-IPs (fig. S6D), caspase-3 and Mex3a were detected using pulldown of biotinylated miR-126-5p from nuclear extracts of rapamycin-treated ECs (Fig. 6E). Analysis of nuclear AGO2-immunodepleted RNA fractions showed that a relevant fraction of the nuclear miR-126-5p pool is not associated with AGO2, and RNA-IP confirmed its interaction with Mex3a or caspase-3 in rapamycin-treated ECs (fig. S6, E and F). The colocalization of caspase-3 with fluorescently tagged synthetic miR-126-5p was reduced by partial (C5 to C8) or full disruption of the seed sequence (Mut1 and Mut2) or more extensive mutation (Mut3) (Fig. 6F). The interaction of recombinant caspase-3 and synthetic miR-126-5p was confirmed by NMR titrations in vitro. Substantial spectral changes of caspase-3 methyl signals upon addition of miR-126-5p (Fig. 6G and fig. S6G) as well as RNA signals upon addition of caspase-3 (fig. S6H) demonstrated direct binding. SPR on immobilized miR-126-5p revealed an equilibrium dissociation constant (K_D) of 1.95 ± 0.30 μM for caspase-3 (fig. S6, I to K). SPR on immobilized caspase-3 p17 subunit revealed binding of miR-126-5p but failed to detect responses with other miRNAs or miR-126-5p mutated in the seed sequence (Mut1 to Mut3), corroborating the specificity of miR-126-5p (fig. S6L).

To verify that miR-126-5p can dissociate from AGO2 in favor of caspase-3, we performed competition assays on immobilized miR-126-5p, showing that caspase-3 displaces AGO2 binding to miR-126-5p (Fig. 6H). Computational modeling further indicated that miR-126-5p may engage in interactions with the substrate-binding pocket and the heterodimer interface of caspase-3. The computed BFEs in silico suggested a privileged binding of miR-126-5p to caspase-3 monomers rather than heterodimers (fig. S6, M to P). Accordingly, SPR revealed that dimerization of caspase-3 p17 subunits was dose-dependently disrupted by miR-126-5p (Fig. 6I). As dimerization of caspase-3 is critical for proper assembly of its active site (*40*), we explored its functional role. In cell-free assays, miR-126-5p dose-dependently reduced substrate cleavage by recombinant caspase-3 with a half maximal inhibitory concentration (IC_{50}) of 14.4 μM comparable to inhibition with benzyloxycarbonyl-Val-Ala-Asp[OMe]-fluoromethylketone

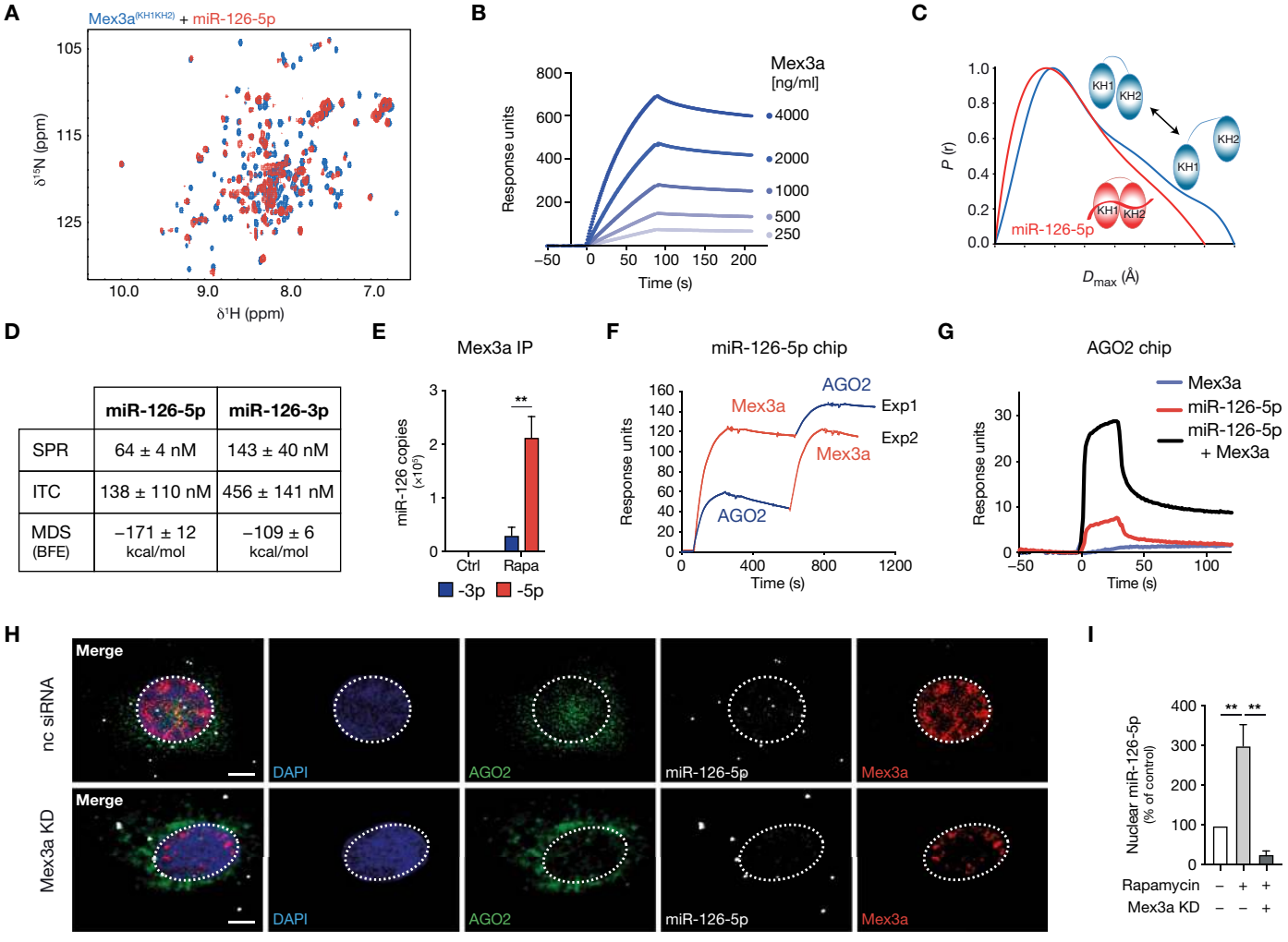

	miR-126-5p	miR-126-3p
SPR	64 ± 4 nM	143 ± 40 nM
ITC	138 ± 110 nM	456 ± 141 nM
MDS (BFE)	−171 ± 12 kcal/mol	−109 ± 6 kcal/mol

Fig. 4. Mex3a preferentially binds miR-126-5p to drive nuclear enrichment. (**A**) Overlay of ^{1}H-^{15}N HSQC spectra of Mex3a$^{(KH1KH2)}$ in the absence (blue cross-peaks) or presence (red) of miR-126-5p (molar ratio, 1:2). (**B**) SPR sensorgram for interaction between immobilized miR-126-5p and full-length Mex3a. $K_D = 3.6 \pm 2.9$ nM. (**C**) Pairwise distance distribution derived from SAXS of Mex3a$^{(KH1KH2)}$ in the absence (blue) or presence (red) of miR-126-5p. (**D**) Table of estimated binding affinity parameters for the interaction of Mex3a with miR-126-5p and miR-126-3p. (**E**) RNA-IP of Mex3a in nuclear lysates of HUVECs treated without (Ctrl) and with rapamycin (Rapa) showing miR-126 strand loading ($n = 3$). (**F**) SPR sensorgrams showing interaction of sequentially loaded full-length recombinant Mex3a and AGO2 (Exp1) and vice versa (Exp2) on immobilized miR-126-5p. (**G**) SPR sensorgrams for full-length Mex3a, miR-126-5p, or their combination perfused on AGO2, showing a marked interaction of Mex3a and AGO2 in a complex with miR-126-5p. (**H**) Representative deconvoluted images for fluorescence in situ hybridization (FISH) for miR-126-5p (gray) and coimmunostaining for AGO2 (green) and Mex3a (red) in rapamycin-treated HUVECs with or without Mex3a KD. Scale bars, 5 μm. (**I**) Amount of nuclear miR-126-5p in HUVECs upon rapamycin and Mex3a silencing ($n = 5$). $^{**}P < 0.01$. Two-factor repeated measures ANOVA (E) or univariate ANOVA with Bonferroni post hoc test (I).

(Z-VAD-FMK) (IC_{50}, 75.9 μM) or benzyloxycarbonyl-Asp[OMe]-Glu[OMe]-Val-Asp[OMe]-fluoromethylketone (Z-DEVD-FMK) (IC_{50}, 2.8 μM) (Fig. 6J), supporting the notion that miR-126-5p interferes with both binding pocket and heterodimer-driven active site formation. In contrast, seed-mutated miR-126-5p (Mut1 to Mut3), miR-126-3p, let-7a-5p, miR-17-5p, and miR-21-5p were ineffective (Fig. 6J and fig. S6Q). Collectively, our data establish that nuclear miR-126-5p guided by Mex3a and after its dissociation from AGO2 can protect ECs from apoptosis by direct inhibition of caspase-3.

Nuclear miR-126-5p:Mex3a pathway is operative in vivo and in human disease

To provide in vivo evidence for the relevance of the autophagy-driven pathway in vascular disease, we analyzed endothelial staining patterns for LC3 en face in aortas of atherosclerosis-prone *Apoe*$^{-/-}$ mice by three-dimensional (3D) deconvolution immunofluorescence. LC3 staining was more prevalent in areas exposed to HSS (i.e., thoracic aorta) versus LSS (i.e., the aortic arch as a predilection site) (Fig. 7, A and B). Because lipoproteins trigger autophagic flux in ECs in vitro (*41*), we analyzed effects of high-fat diet (HFD). Preserving a preferential activation in the thoracic aorta, HFD for 12 but not for 4 weeks significantly increased endothelial LC3 staining ($P = 0.0016$) (Fig. 7, A and B). Moreover, nuclear LC3 localization was less common and the percentage of nuclear Ago2^{+} ECs was lower in areas of LSS, namely, in the inner curvature of the aortic arch, than in those of HSS (Fig. 7, C to E). Endothelium of nondiseased human carotid arteries upstream of the bifurcation (exposed to HSS) showed more prominent nuclear AGO2 localization than atheromatous areas with disturbed flow

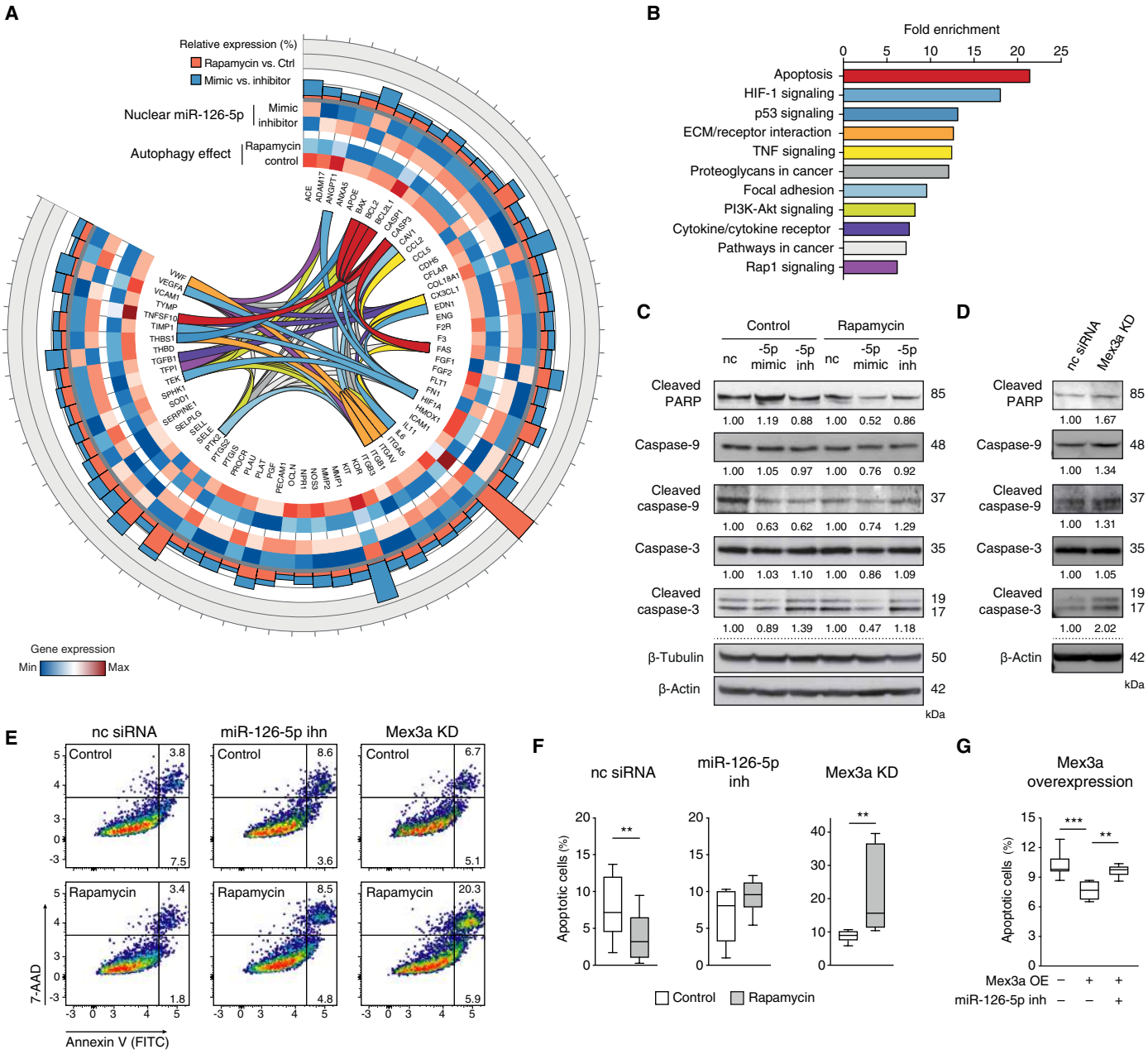

Fig. 5. Nuclear miR-126-5p inhibits apoptosis. (**A**) Circos plot showing changes in EC-relevant genes induced by rapamycin and miR-126-5p. Heat maps show relative expression in rapamycin-treated HUVECs versus controls (inner) and cells treated with rapamycin and miR-126-5p mimic or inhibitor (outer). KEGG functional categories are indicated by ribbons and (**B**) ranked according to fold enrichment. HIF-1, hypoxia-inducible factor 1; ECM, extracellular matrix; TNF, tumor necrosis factor. (**C**) Western blot analysis of apoptosis mediators in controls and rapamycin-treated HUVECs with gain- or loss-of-function for miR-126-5p or (**D**) after Mex3a KD versus control siRNA (nc) including normalized densitometry analysis. PARP, poly(ADP-ribose) polymerase. (**E**) Representative flow cytometry analysis and (**F**) quantification of apoptosis rates (percentage of annexin V$^+$ cells) after rapamycin treatment for 3 hours ($n = 10$) and miR-126-5p inhibition (-5p inh) ($n = 10$) or Mex3a KD ($n = 10$) and (**G**) upon Mex3a overexpression with or without miR-126-5p inhibitor ($n = 7$). 7-AAD, 7-aminoactinomycin D; FITC, fluorescein isothiocyanate. $^{**}P < 0.01$ and $^{***}P < 0.001$. Mann-Whitney *U* test (F) or univariate ANOVA (G) with Bonferroni post hoc test.

downstream of the bifurcation (LSS) (Fig. 7, F and G). Moreover, confocal deconvoluted microscopy unveiled closely localizing signals for Mex3a and miR-126-5p in the nucleus of ECs (Fig. 7H). We quantified the closest distance between Mex3a and miR-126-5p in EC nuclei as a proxy of interaction and found that this distance appears to be lower in ECs of undiseased vascular areas than in ECs overlying atherosclerotic lesions, thus reflecting a higher probability of interaction (Fig. 7, I and J). Together, these findings extend the relevance of our results to human disease.

We next evaluated *Apoe*$^{-/-}$*Cdh5*$^{Cre+}$*Atg5*$^{fl/fl}$ (ATG5$^{EC\text{-}KO}$) mice with defective endothelial autophagy (*42*). After 12 weeks of HFD, the percentage of ECs with nuclear Ago2 and miR-126-5p signals (as assessed by in situ PCR) in the thoracic aorta (Fig. 7, K to L, and

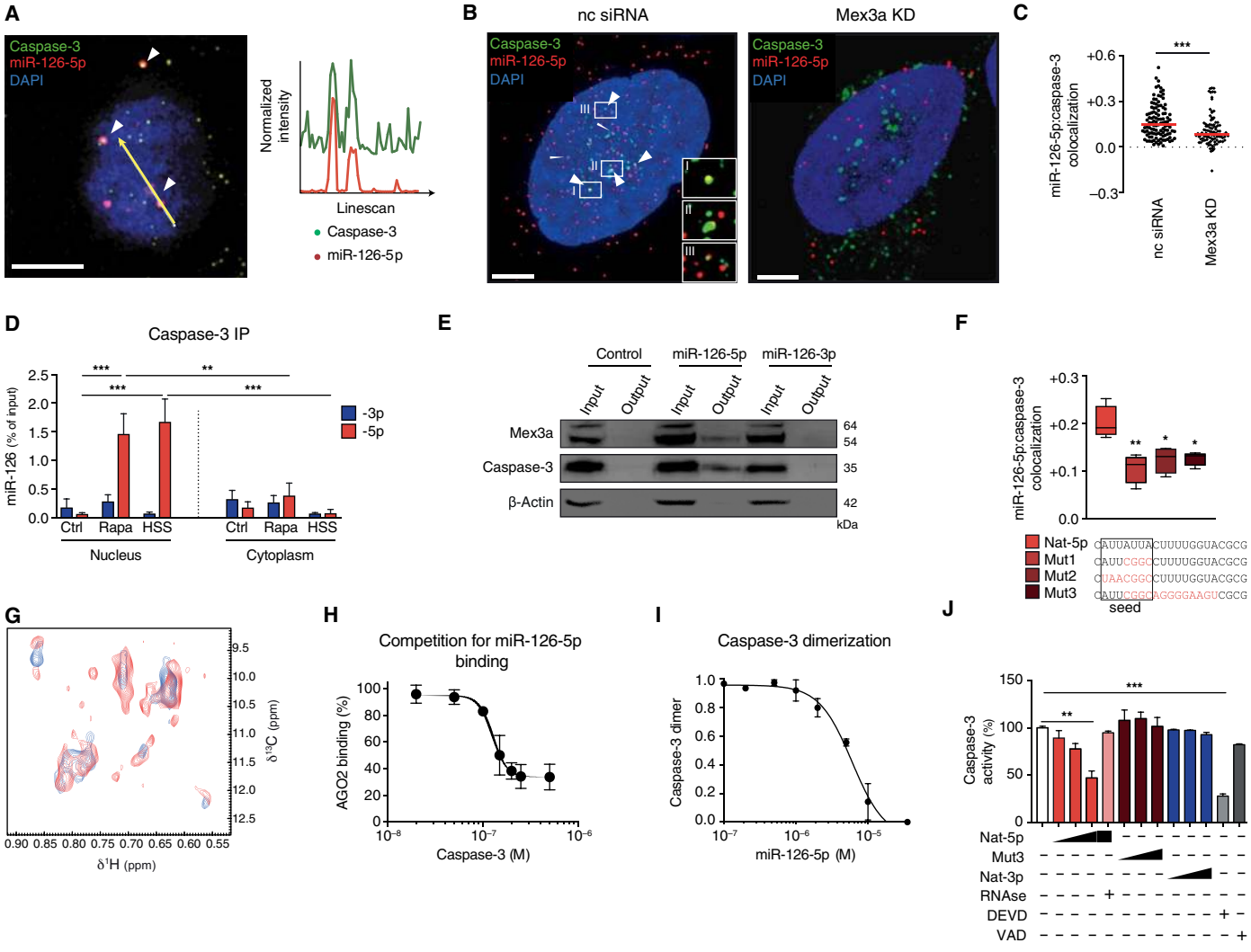

Fig. 6. miR-126-5p interacts with caspase-3 to inhibit its activity. (**A**) Representative deconvoluted image for FISH for miR-126-5p (red) and coimmunostaining for caspase-3 (green) showing colocalizing signals in nucleus and perinuclear area (white arrowheads). Plot shows normalized fluorescence intensity profiles for green and red channels in the position marked by orange arrow. Scale bar, 5 μm. (**B**) Representative deconvoluted images for FISH for miR-126-5p and coimmunostaining for caspase-3 in rapamycin-treated HUVECs transfected with nonspecific siRNA (nc siRNA) or siRNA against Mex3a (Mex3a KD) and (**C**) Pearson's coefficients for caspase-3 and miR-126-5p colocalization, red line denotes median ($n = 100$ to 110). (**D**) RNA-IP of nuclear and cytoplasmic caspase-3 for miR-126 strand loading in HUVECs treated with rapamycin ($n = 6$) or exposed to laminar shear stress (HSS, 12 dyne/cm^2) ($n = 3$) and controls ($n = 9$). (**E**) Biotin-RNA pulldowns of miR-126 strands transfected in HUVECs showing interaction with Mex3a and caspase-3 after rapamycin treatment. (**F**) Pearson's coefficient for miR-126-5p mutants and caspase-3 colocalization in rapamycin-treated HUVECs ($n = 4$). Sequences of native miR-126-5p (Nat-5p) and mutants (Mut1 to Mut3) are given below. Red denotes mutated nucleotides. (**G**) Superposition of two-dimensional NMR spectra of $^1H^{13}C$ methyl ILVM, ^2H-labeled caspase-3 (blue) and in complex with miR-126-5p (red), molar ratio 1:3. (**H**) Competition-binding assay using AGO2 and caspase-3 on immobilized miR-126-5p ($n = 3$). $IC_{50} = 126.9$ nM. (**I**) Competition-binding assay using caspase-3 monomer and miR-126-5p ($n = 3$). $IC_{50} = 6.0$ μM. (**J**) Cell-free analysis of caspase-3 activity in presence of miR-126-5p (Nat-5p), miR-126-5p mutant (Mut3), miR-126-3p (Nat-3p) (4, 8, or 16 μM), RNAse, the caspase-3 inhibitors Z-DEVD-FMK (DEVD), or Z-VAD-FMK (10 μM) ($n = 3$). *$P < 0.05$, **$P < 0.01$, ***$P < 0.001$. Factorial (D and J) or univariate ANOVA (F) with Bonferroni post hoc test.

fig. S7, A and B) and the content of nuclear miR-126-5p (as determined by qPCR) in both areas of LSS and HSS (Fig. 7M) was lower in ATG5$^{EC\text{-}KO}$ mice than in controls. Increased circulating CD31$^+$ annexin V$^+$ ABs and miR-126-3p concentrations (*19*) implied enhanced EC apoptosis in ATG5$^{EC\text{-}KO}$ mice (Fig. 7N and fig. S7, C and D). As apoptosis disrupts endothelial integrity to promote atheroprogression (*8*, *16*, *17*, *43*), the burden of atherosclerosis was accordingly increased in ATG5$^{EC\text{-}KO}$ mice after 12 weeks of HFD (Fig. 7O), an effect due to a prominent exacerbation in areas of HSS (Fig. 7P). As another approach to prevent nuclear enrichment of miR-126-5p in vivo, we generated mice with a genetic deficiency of *Mex3a* (fig. S7E). Similar to ATG5$^{EC\text{-}KO}$ mice, the thoracic aorta of *Mex3a*$^{-/-}$ mice displayed fewer ECs with nuclear Ago2 staining (Fig. 7Q and fig. S7F), and in situ RNA hybridization revealed a marked reduction in nuclear miR-126-5p$^+$ ECs (Fig. 7, R and S). Conversely, nuclear staining for caspase-3, reflecting the active form, was increased in *Mex3a*$^{-/-}$ mice (Fig. 7T and fig. S7G) and, consistent with enhanced endothelial apoptosis, confirmed in *Mex3a*$^{-/-}$ pulmonary ECs (fig. S7H). In human carotid artery samples, close localized signals for miR-126-5p and caspase-3 were detectable with a higher prevalence

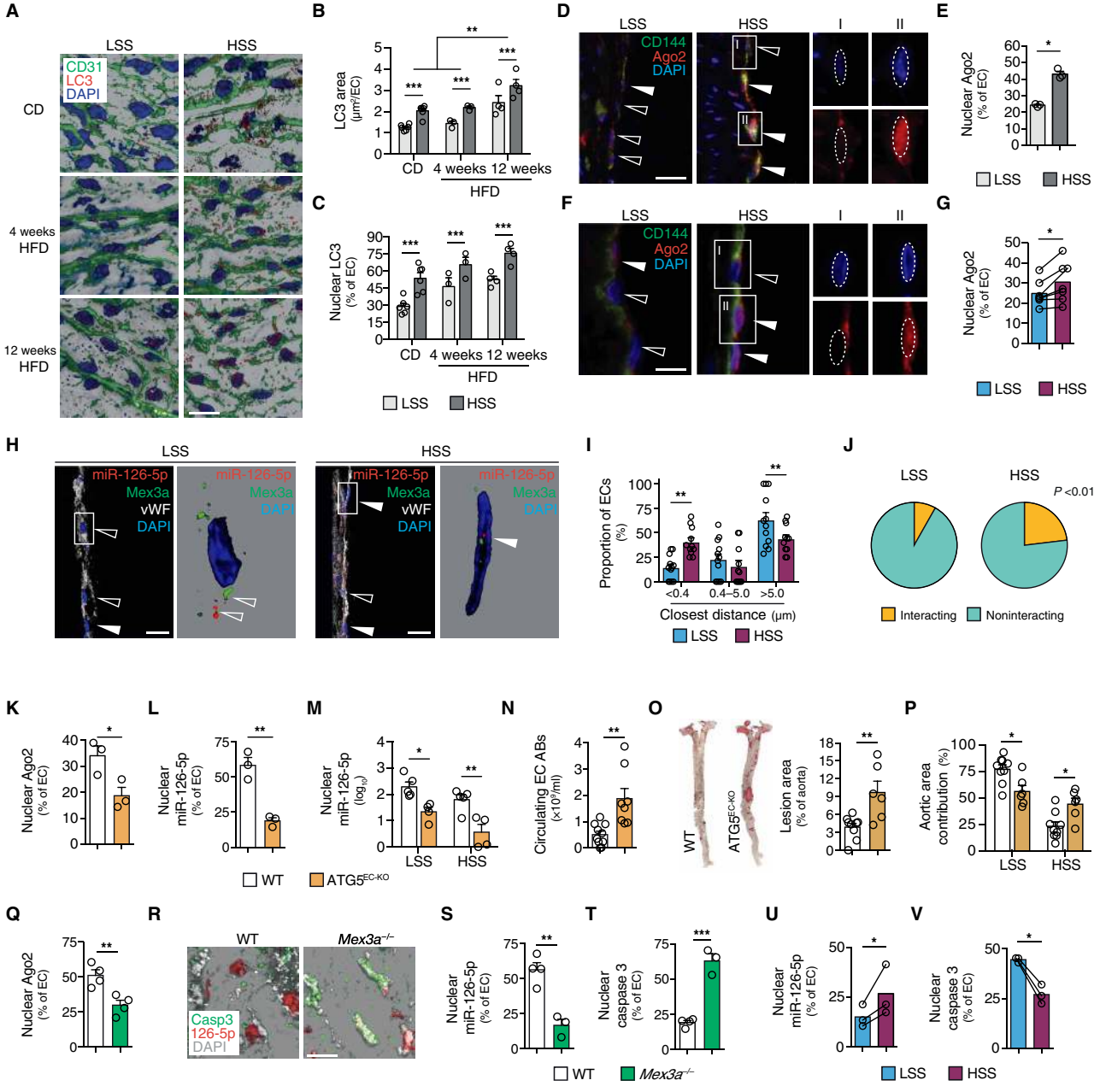

Fig. 7. Deleting *Atg5* or *Mex3a* attenuates nuclear miR-126-5p-AGO2 shuttling to drive endothelial apoptosis and atherosclerosis in vivo. (**A**) 3D deconvolution microscopy with (**B**) quantification of $LC3^+$ area and (**C**) percentage of ECs showing nuclear LC3 in en face aortic arch [low shear stress (LSS)] versus thoracic aorta [high shear stress (HSS)] of $Apoe^{-/-}$ mice ($n = 3$ to 6) fed chow (CD) or high-fat diet (HFD) for 4 to 12 weeks. Scale bar, 20 μm. (**D** to **G**) Immunofluorescence and percentage of ECs showing nuclear AGO2 in (D and E) aortic arch (LSS) and thoracic aorta (HSS) of $Apoe^{-/-}$ mice ($n = 3$) on HFD for 12 weeks or in (F and G) human carotid artery specimens collected upstream (HSS) or downstream (LSS) of the bifurcation ($n = 7$). Regions I and II in (D and F) are magnified in insets to show single channel details for ECs without (I or empty arrowheads) and with (II or filled arrowheads) nuclear AGO2. Scale bar, 20 μm. (**H**) Confocal deconvoluted microscopy for Mex3a immunostaining and FISH for miR-126-5p in the nucleus of ECs stained for von Willebrand factor (vWF) in human carotid artery specimens upstream (HSS) or downstream (LSS, covering atheroma) of the bifurcation ($n = 3$). Regions in the box are magnified on the right. Scale bars, 20 μm. (**I**) The closest distance between Mex3a and miR-126-5p in EC nuclei was quantified in 12 fields of view per region. Distributions are shown for overall distances and (**J**) for a proxy of interaction defined by a distance below the resolution limit of 240 nm. (**K** to **P**) Characterization of $Apoe^{-/-}Cdh5^{Cre+}Atg5^{fl/fl}$ ($ATG5^{EC\text{-}KO}$) and $Apoe^{-/-}Cdh5^{Cre-}Atg5^{fl/fl}$ WT mice on HFD for 12 weeks. (K) Percentage of ECs showing nuclear AGO2 (immunofluorescence) and (L) miR-126-5p (in situ PCR) in thoracic aorta ($n = 3$). (M) Nuclear expression of miR-126-5p in aortic arch (LSS) versus thoracic aorta (HSS) ($n = 4$ to 5). (N) Circulating endothelial ABs in plasma ($n = 8$ to 10). (O) Atherosclerotic lesion area in Oil-red-O-stained aortas and (P) fractional contribution of aortic arch (LSS) and thoraco-abdominal aorta (HSS) ($n = 6$ to 9). (**Q**) Percentage of thoracic aortic ECs showing nuclear AGO2 in C57Bl6/NCrl (WT) and $Mex3a^{-/-}$ mice ($n = 4$). (**R**) FISH for miR-126-5p and coimmunostaining for caspase-3 and CD31 in en face thoracic aorta from WT and $Mex3a^{-/-}$ mice. Scale bar, 20 μm. (**S**) Percentage of ECs showing nuclear miR-126-5p and (**T**) caspase-3 ($n = 3$ to 4). (**U**) Percentage of ECs showing nuclear miR-126-5p and (**V**) caspase-3 in human carotid artery specimens downstream (LSS) or upstream (HSS) of the bifurcation ($n = 3$). $^*P < 0.05$, $^{**}P < 0.01$, $^{***}P < 0.001$. Two-factor repeated measures ANOVA (B and C) or factorial ANOVA (I, M, and P) with Bonferroni post hoc test, paired *t* test (E, G, U, and V), unpaired Student's *t* test (K, L, N, O, Q, S, and T), or Fisher's χ^2 test (J).

in nondiseased versus atheromatous areas (Fig. 7, U and V, and fig. S7, I to J). Collectively, our data support that the nuclear Ago2:Mex-3a:miR-126-5p pathway driven by endothelial autophagy can occur in vivo to confer shear-dependent atheroprotection.

DISCUSSION

Our study unravels an unexpected miRNA function by establishing that nuclear miR-126-5p inhibits proapoptotic caspase-3 activity through a direct miRNA-protein interaction. This noncanonical mechanism involves a specific Mex3a-guided nuclear transfer of miR-126-5p (fig. S7K). This expands the known spectrum of posttranscriptional regulation by miRNAs and adds an unexpected mechanism to the repertoire of antiapoptotic armor for protecting and maintaining EC integrity in the context of autophagy.

The role of Mex3a in mammals is largely unknown but it has been correlated to stemness in colon cancer cell lines (*36*) and in a subpopulation of slowly proliferating intestinal progenitor cells (*44*). Mex3a was identified and characterized as an RNA binding protein that shuttles between the nucleus and the cytoplasm, where it colocalizes with AGO2 (*35*). While ribonuclease (RNAse) could disrupt the interaction with AGO2, the nature of this bridging RNA remained to be defined. Our results reveal that Mex3a can bind to miRNAs through its KH domains, featuring a remarkable preference for miR-126-5p. The presence of miR-126-5p is required for the formation of a ternary complex with Mex3a and AGO2 without a target mRNA, as it may occur in LMW complexes under conditions of autophagy.

AGO2 uses guide miRNAs to interrogate mRNAs targeted for posttranscriptional repression. The crystal structures of AGO2 bound to a guide miRNA with and without target RNA suggest a stepwise mechanism, in which AGO2 primarily exposes guide nucleotides 2 to 5 in the 5′ end for initial target pairing, thereby promoting conformational changes that expose nucleotides 2 to 8 and 13 to 16 for further target recognition (*45*, *46*). In the regular guide, the 5′ end stretches across in the central cleft between the two AGO2 domains (N-PAZ and MID-PIWI) and is restricted after nucleotide 8, while the 3′ end is threaded through the N-PAZ channel. Ternary complex formation of AGO2, Mex3a, and miR-126-5p may thus involve an interaction of the 5′ region of miR-126-5p with AGO2, whereas the Mex3a tandem KH domains may engage in contact with the 3′ part of miR-126-5p not bound to AGO2. In addition, direct interactions between AGO2 and other regions in Mex3a, outside the RNA binding KH domains, might occur to further stabilize the ternary complex.

The mechanism by which Mex3a directs miR-126-5p toward the nucleus upon binding and ternary complex formation with AGO2 remains elusive. The interaction with Mex3a may support retention of the complex on the external surface of the autophagosome and transfer to the nuclear pore for importin interaction. As a limitation of our study, it remains to be determined whether and which additional adaptor(s) may contribute to the interactions of the complex with LC3. The protein LC3 plays an important role in the selective recruitment of autophagic cargo and can thus serve as docking site for multiple adaptor proteins, which can simultaneously interact with LC3 in autophagosomes and with their cargo (*47*). Hence, one would need to postulate such components to anchor and present the Mex3a:AGO:miR-126-5p complex on the extraluminal autophagosome membrane for nuclear import, as indicated by the absence of LC3 in AGO2 immunoprecipitates. Additional components may support the LC3:AGO2 interaction in a manner sufficient to detect a proximity by STED nanoscopy but not a presence of LC3 in AGO2 immunoprecipitates. Because mutational changes involving nucleotides 2 to 8 in the 5′ end of miR-126-5p do not affect nuclear enrichment, it is conceivable that binding of both 3′ and 5′ parts of miR-126-5p to the KH domains of Mex3a is dispensable for nuclear transfer. The importin-dependent nuclear localization sequence predicted with the highest score is located in the RING domain (residues 417 to 445) of Mex3a. Likewise, further efforts are warranted to identify protein or RNA components in the nucleus that enable the dissociation of miR-126-5p from AGO2 in favor of caspase-3 and to release the seed sequence required for its interaction with caspase-3. Our data indicate that Mex3a facilitates this process, as evidenced by reduced nuclear colocalization upon its silencing.

Autophagy is integral to the well-orchestrated programs of cellular responses to stress. Many triggers of autophagy can also induce apoptosis with both processes often occurring in the same cell (*48*). Apoptosis is a modality of programmed cell death mediated by specific cascades of proteases, which culminate in the activation of effector caspases (e.g., caspase-3) responsible for killing the cells (*49*). Given the antagonistic role of the two processes, autophagy being cytoprotective and apoptosis being cytodestructive, it appears teleologically conceivable that an inhibitory cross-talk exists. For example, removal of damaged mitochondria or proapoptotic proteins during autophagy inhibits apoptosis, whereas caspase-3 may cleave autophagy-specific proteins to impair autophagy (*48*). Our results establish a mechanism by which autophagy can inhibit apoptosis via miR-126-5p. This inhibition mainly affects caspase cleavage rather than expression and its rapid onset preceded transcriptional changes, prompting our hypothesis that miR-126-5p directly acts on effector caspases. Among those, caspase-3 is essential for nuclear changes upon apoptosis and localizes in the nucleus after activation and recognition of substrates, independently of their cleavage (*39*). In this compartment, the interaction with miR-126-5p may prevent catalysis of nuclear components to preserve cell viability. The inhibition of apoptosis by directly controlling catalytic activity of caspase-3 is typically exerted by protein-protein interactions. Our results integrate and extend the pathophysiological relevance of related findings showing that: (i) miRNAs can adopt a stable secondary structure resembling aptamers, short oligonucleotide sequences with high affinity for molecular targets including proteins (*50*); (ii) miRNAs and AGO2 frequently localize in LMW complexes devoid of functional RISC components to form miRNA reservoirs in vivo (*5*); and (iii) the conserved noncoding RNA *vtRNA1-1*, termed riboregulator, can prevent oligomerization of the protein p62, thus altering its function in autophagy (*51*).

Although we show that miR-126-5p engages in interactions with caspase-3 to inhibit its proapoptotic activity in vitro and in ECs, the molecular mechanisms underlying this effect remain to be deciphered in detail. As the four loops forming the active site are provided by both heterodimer subunits, dimerization is crucial for proper assembly and cooperativity of active sites in all caspases (*40*). MDS implied that miR-126-5p preferentially binds to caspase-3 monomers rather than to heterodimers. Dimerization of the p17 caspase-3 subunit could be inhibited by miR-126-5p in vitro. On the other hand, MDS predicted that the 5′ end (containing the seed sequence) of miR-126-5p may bind the substrate binding pocket with strong affinity, whereas mutational changes involving nucleotides 2 to 8 impair the inhibitory activity. Although it will be crucial to dissect the precise mechanism of inhibition, it is plausible from our data that miR-126-5p may affect

caspase-3 activity by a dual mechanism, (i) disrupting dimerization and (ii) preventing substrate binding at its pocket. For pro–caspase-3, the first cleavage by activator caspases disrupts the covalent link between the p17 and p12 subunits. Although p12 remains associated by noncovalent binding, conformational changes occurring as a result of this cleavage may also be targeted by interactions with miR-126-5p.

We found that rapamycin-transferred nuclear miR-126-5p was associated with altered transcript expression of apoptosis-related genes. These changes occurred later than the antiapoptotic effect detected by annexin V staining. Whereas direct inhibition of caspase-3 activity explains early onset, subsequent changes in gene expression may serve to stabilize antiapoptotic effects of miR-126-5p. Nuclear miRNAs can affect gene expression by several mechanisms including post-transcriptional and transcriptional regulation, alternative splicing, or epigenetic modifications (*38*). As most of these processes require AGO2 and other RISC components (such as TNRC6A), this is likely mediated by the AGO2-bound fraction of miR-126-5p.

Although the mechanism identified herein could be potentially operative in every cell, the remarkable abundance of miR-126-5p in ECs compared to other cell types (*52*) indicates that it mainly serves as a critical master switch to control programmed cell death in ECs. Endothelial apoptosis plays a pivotal role in atherosclerosis, and a higher apoptosis rate has been found in areas exposed to LSS in mice and humans (*8*, *43*). Conversely, activation of KLF2 and autophagic flux as well as miR-126-5p amounts were significantly reduced in those areas, due to the absence of HSS (*8*, *13*, *16*). Our results merge and complement these observations by identifying a common functional pathway preserving endothelial integrity. Overexpression of KLF2 recapitulated the initiation of autophagic flux and the preferential up-regulation of miR-126-5p observed upon HSS, thus supporting a role of KLF2 as an important relay between HSS and initiation of autophagy.

Endothelial autophagy is required for maintaining lipid homeostasis (*41*) and for ensuring proper alignment to flow (*8*). Deficiency in EC autophagy (conditional *Atg7/Atg5* knockout) resulted in more severe atherosclerosis, prevalently at sites exposed to HSS (*8*, *41*). The higher rate of apoptosis described in aortic ECs of these mice (*8*) is paralleled by our findings showing an impaired nuclear enrichment of miR-126-5p and thus support its involvement in preserving endothelial integrity in vivo. Consistently, impeding nuclear transfer of miR-126-5p through another strategy such as silencing *Mex3a* led to higher apoptosis rates in ECs. Future work will scrutinize in detail how genetic deficiency of Mex3a in a cell-specific context may affect the initiation and progression of atherosclerosis.

We previously found that miR-126-5p preserves the endothelial proliferative reserve during hyperlipidemia by repressing a negative regulator of proliferation, *Dlk1* (*16*). Maintenance of endothelial integrity requires the replacement of damaged ECs by proliferating ones. At arterial sites exposed to HSS, miR-126-5p does not only promote regenerative proliferation by targeting *Dlk1* mRNA in the RISC but, as shown herein, it may also preserve EC viability by attenuating apoptotic cell death, when enriched in the nucleus via an autophagy-driven mechanism. In line with higher autophagic activity during HFD, as reflected by LC3 staining, this feature would conceivably be more effective when the baseline regenerative equilibrium is disrupted by additional endothelial injury, e.g., during dyslipidemia. Although we currently do not know whether these events occur simultaneously or in a sequential manner—for example, *Dlk1* mRNA decay followed by nuclear transfer and inhibition of caspase-3—this will be of both scientific and potentially clinical interest. Use of rapamycin or other mTOR inhibitors to prevent restenosis is limited by defective reendothelialization, possibly due to mTORC2 inhibition (*53*). Thus, emulating the antiapoptotic downstream pathway involving Mex3a–miR-126-5p might enable more specific and hence safer therapeutic options in this context.

We foresee a possible therapeutic relevance in promoting nuclear enrichment of miR-126-5p to prevent endothelial dysfunction and development of atherosclerosis as well as in other conditions where viability of the endothelium is crucial for cardiovascular outcomes (e.g., reendothelialization after acute cardiovascular events). To this end, a tailored overexpression of Mex3a could be achieved by using endothelial-specific constructs in viral microparticle, which can be delivered systemically or locally. Although additional studies will be required to verify such hypotheses, we believe that this approach may be suitable to improve the antiatherosclerotic effects previously achieved by systemic administration of nanoparticles carrying miR-126-5p (*16*).

Although nuclear miR-126-5p could potentially act as a diagnostic marker of endothelial health, its evaluation would require sophisticated analysis of pathological specimens by FISH and is thus unlikely to enhance the diagnostic performance of current tests. On the other hand, quantification of circulating $CD31^+$ ABs could reflect the amount of distressed ECs and act as a surrogate marker (or prognostic factor) in cardiovascular disease (*54*). Yet, a validation of the diagnostic performance would require further investigations on large prospective cohorts.

Our data also reinforce the notion that proteins relevant for cell viability (caspase-3 or p62) have previously escaped recognition as RNA binding proteins (*51*, *55*). The Mex3a:miR-126-5p shuttle operates downstream of EC autophagy and can thus integrate crucial effector mechanisms, limiting atherosclerosis and its complications. However, the spectrum of human disease wherein autophagy governs the equilibrium between cell death and survival ranges from aging to cancer and neurodegenerative diseases (*6*, *7*, *11*, *56*). In addition, the proper functionality of the endothelium is required for angiogenesis in health and disease (*57*). Thus, modulating or emulating this pathway composed of sequential miRNA-protein interactions to restore endothelial functionality unfolds multiple options for therapeutic targeting in vascular disease and beyond.

MATERIALS AND METHODS

Study design

The main objective of our study was to identify noncanonical mechanisms of miRNA function. We took advantage of the peculiarity of endothelial miR-126 with both strands active, and we investigate mechanisms of strand-specific sorting. We focus on autophagic conditions which favor the recruitment of AGO2:miRNAs in LMW complexes devoid of silencing effector components (e.g., TNRC6A). Experiments in vitro in HUVECs involved manipulation of autophagic flux by chemical inducers and inhibitors (rapamycin, 3-methyladenine, and bafilomycin) or gene manipulation [KLF2 overexpression and small interfering RNAs (siRNAs) against ATG5/ATG7] for (i) multimodal tracking miR-126 strands (fractional qPCR, FISH, and fluorescently tagged miRNAs), (ii) identification of interacting proteins that mediate trafficking and functional outcomes (i.e., RNA-IP, IP, size exclusion chromatography, and immunostainings), and (iii) analysis of downstream effects (qPCR and immunoblotting for relevant mediators and assessment of apoptosis). Protein-RNA interactions were detailed in silico and by biophysical experiments (SPR, SAXS,

and NMR spectroscopy). Moreover, the functional relevance was tested (competition and caspase-3 activity assays). Last, the pathophysiological significance was tested in vivo in transgenic mice models disrupting the identified pathway at different layers (ATG5$^{EC\text{-}KO}$ and *Mex3a*$^{-/-}$), studying atherosclerosis as a disease model relevant for EC autophagy and miR-126.

In vitro experiments in ECs

HUVECs were treated with rapamycin (Santa Cruz Biotechnology) at 5 μM, ivermectin (Santa Cruz Biotechnology) at 10 mM, 3-methyladenine (Sigma-Aldrich) at 5 mM, bafilomycin (Enzo Life Sciences) at 160 nM, and/or camptothecin (Abcam) at 500 nM. Unless stated otherwise, treatment was applied for 3 hours to analyze early processes and to avoid activation of concomitant or compensatory mechanisms. RNA interference technology was applied to generate specific knockdowns with siRNA against ATG5, ATG7, and Mex3a (Qiagen). Functional studies on miRNA function were carried with miScript miRNA mimics and inhibitors of miR-126-5p (Qiagen). Overexpression of KLF2 and Mex3a were obtained by pCMV-hKLF2 and pCMV-hMex3a plasmids. Transfections were performed by electroporation using Amaxa Nucleofector technology (Lonza) or Lipofectamine 2000 (Thermo Fisher Scientific) according to the manufacturer's protocols. All antibodies and primers used in the experiments are detailed in tables S2 and S3.

In silico protein-miRNA docking and MDS

The potential binding modes between miR-126-3p and miR-126-5p with Mex3a and caspase-3 were predicted by application of protein-RNA docking using HDOCK and HADDOCK webserver (*58*, *59*). The selected docking poses were subjected to 20-ns MDS. Trajectories extracted from 15 to 20 ns were used for calculating BFE with molecular mechanics/generalized Born surface area by applying default parameters and generalized Born model 8 for free energy of solvation as described (*60*, *61*). To analyze the stability of binding between Mex3a and miR-126-3p and miR-126-5p, MDS of the final complexes were performed for another 180 ns and MD snapshots from different time points were extracted for BFE calculations.

Biophysical and biochemical in vitro studies

SPR experiments were performed using a Biacore X100 (GE Healthcare) using streptavidin (SA) chips, as described (*60*). Sensorgrams were obtained by injecting different concentrations of analytes over the chips. Responses from analyte injections were overlaid with the fit of a 1:1 Langmuir interaction model. For competition assays, the IC_{50} was determined using a four-parameter logistic regression.

SAXS experiments on Mex3a$^{(KH1KH2)}$ or the Mex3a$^{(KH1KH2)}$–miR-126-5p complex were performed with a Rigaku BioSAXS1000 system and a microfocus rotating anode (Cu-Ka 0.154 nm, 40 kV, 30 mA). A Pilatus 100k detector was used for image collection, and a built-in photo diode was used for transmission measurements. The Rigaku SaxsLab software 3.1 was used for radial averaging, q calibration, and solvent subtraction. Radiation damage, data merging, and buffer subtraction were performed on site and later verified manually using the program PRIMUS (*62*). All SAXS parameters such as maximum particle size (D_{max}) were extracted using the GNOME from the ATSAS package software (*63*). Statistics on SAXS data collection and analysis are reported in table S4.

ITC experiments were performed using a MicroCal ITC200 instrument (Malvern). Both Mex3a$^{(KH1KH2)}$ and RNA (miR-126-5p and miR-126-3p) were dissolved in PBS buffer at pH 6.5. Mex3a$^{(KH1KH2)}$ (200 μl) at a concentration of 20 μM was titrated with the two RNA ligands at 200 μM concentration at 25°C. For each ITC experiment, a background curve consisting of the titration of the same RNA sample into buffer was subtracted to account for heat generated by dilution. Measurements were carried out in triplicates. The MicroCal PEAQ-ITC (Malvern) software was used to analyze all ITC data. As the binding isotherms suggest a more complex binding event, an estimation of the binding affinity was obtained by only fitting the second part of the curve, as this is expected to report on the RNA binding to Mex3a. The complex binding isotherm likely represents a structural rearrangement of the two KH domains upon RNA binding, as indicated by the SAXS data.

NMR spectroscopy was performed at 600- or 800-MHz spectrometers equipped with cryoprobes. ^{15}N-labeled Mex3a$^{(KH1KH2)}$ was concentrated to 100 μM and titrated with miR-126-5p or mir-126-3p added at 1:0.5, 1:1, and 1:2 stoichiometry. $^{1}H^{13}C$ methyl isoleucine, leucine, valine, methionine, ^{2}H-labeled caspase-3 was concentrated to 20 μM, and miR-126-5p was added at threefold molar excess. NMR spectra were processed with NMR Pipe/NMR Draw (*64*) and analyzed using NMR View (*65*). ^{1}H NMR spectra of caspase-3 free and bound to miR-126-5p RNA were analyzed with Topspin.

Animal experiments

Mice with EC-specific deletion of *Atg5* (*Cdh5*$^{Cre+}$*Atg5*$^{fl/fl}$) were recently described (*42*) and crossed with *Apoe*$^{-/-}$ mice to obtain *Apoe*$^{-/-}$*Cdh5*$^{Cre+}$*Atg5*$^{fl/fl}$ (termed ATG5$^{EC\text{-}KO}$) mice. Age- and sex-matched control animals were used for in vivo experiments. A constitutive knockout model for Mex3a was generated by CRISP-Cas9 genome editing, as detailed in the Supplementary Materials. All animal experiments were approved by the local authorities (District Government of Upper Bavaria, Germany; license number: 55.2-1-54-2532-14-15) and conducted in accordance with the institutional and national guidelines for the care and use of laboratory animals.

A comprehensive and more detailed description of all experimental procedures can be found in the Supplementary Materials.

Statistical analysis

Data were analyzed using the Prism 8 (GraphPad Inc.) and SPSS v.25 (IBM Corp). Descriptive statistics included mean and SEM, unless differently indicated. For box plots, center line represents the median; box limits, Q1 and Q3 quartiles; whiskers, 1.5× interquartile range; points, eventual outliers. For animal experiments: a priori calculation of power was performed on the basis of previous data in literature and pilot experiments. Sample size was designed to achieve 80% power for detecting biological relevant changes (50%) with an α-value of 0.05. For in vitro experiments, sample sizes were selected empirically on the basis of pilot experiments. Data distribution and homogeneity of variance were tested by the Shapiro-Wilk and Levene's tests, respectively. Violation of the assumptions was considered at $P < 0.05$. Comparisons between two groups were performed by Student's *t* test, with Welch correction as appropriate, or not-parametric Mann-Whitney *U* test. Depending on the number of factors involved, univariate or factorial analysis of variance (ANOVA) with Bonferroni post hoc tests were applied to assess significance in comparisons among three or more groups. Experimental design requiring pairing were analyzed by paired *t* test (two groups) or by two-factor paired measurement ANOVA or by generalized linear model and Bonferroni corrections for pairwise comparisons (≥3 groups). Differences in

proportions were assessed by a Fisher's χ^2 test. The statistical test and the n values are reported in the respective figure legends. Differences were deemed significant at two-tailed $P < 0.05$. Individual subject-level data are provided in data file S1.

SUPPLEMENTARY MATERIALS

stm.sciencemag.org/cgi/content/full/12/546/eaaz2294/DC1
Materials and Methods
Fig. S1. Transcriptional effects of KLF2 and shear stress on ATGs.
Fig. S2. Effect of short-term rapamycin treatment on miR-126 strand release and miR-126 strand-specific transcripts expression and distribution.
Fig. S3. Autophagy promotes nuclear enrichment of AGO2 and Mex3a.
Fig. S4. Basis for computational modeling for generation of homology models for Mex3a KH domains and MDS of interactions with miR-126.
Fig. S5. Mex3a preferentially binds miR-126-5p.
Fig. S6. miR-126-5p interacts with caspase-3.
Fig. S7. Impeding nuclear Ago2:miR-126-5p transfer promotes apoptosis in vivo.
Table S1. BFEs for caspase-3-miRNA interaction.
Table S2. List of antibodies.
Table S3. qPCR primer sets.
Table S4. SAXS data collection and analysis.
Data file S1. Primary data.
References (*66*–*78*)
View/request a protocol for this paper from *Bio-protocol*.

REFERENCES AND NOTES

1. D. P. Bartel, Metazoan MicroRNAs. *Cell* **173**, 20–51 (2018).
2. L. F. R. Gebert, I. J. MacRae, Regulation of microRNA function in animals. *Nat. Rev. Mol. Cell Bio.* **20**, 21–37 (2019).
3. A. K. L. Leung, The whereabouts of microRNA actions: Cytoplasm and beyond. *Trends Cell Biol.* **25**, 601–610 (2015).
4. S. H. Olejniczak, G. La Rocca, J. J. Gruber, C. B. Thompson, Long-lived microRNA–Argonaute complexes in quiescent cells can be activated to regulate mitogenic responses. *Proc. Natl. Acad. Sci. U.S.A.* **110**, 157–162 (2013).
5. G. La Rocca, S. H. Olejniczak, A. J. González, D. Briskin, J. A. Vidigal, L. Spraggon, R. G. DeMatteo, M. R. Radler, T. Lindsten, A. Ventura, T. Tuschl, C. S. Leslie, C. B. Thompson, In vivo, Argonaute-bound microRNAs exist predominantly in a reservoir of low molecular weight complexes not associated with mRNA. *Proc. Natl. Acad. Sci. U.S.A.* **112**, 767–772 (2015).
6. B. Levine, G. Kroemer, Biological functions of autophagy genes: A disease perspective. *Cell* **176**, 11–42 (2019).
7. J. M. B.-S. Pedro, G. Kroemer, L. Galluzzi, Autophagy and mitophagy in cardiovascular disease. *Circ. Res.* **120**, 1812–1824 (2017).
8. A.-C. Vion, M. Kheloufi, A. Hammoutene, J. Poisson, J. Lasselin, C. Devue, I. Pic, N. Dupont, J. Busse, K. Stark, J. Lafaurie-Janvore, A. I. Barakat, X. Loyer, M. Souyri, B. Viollet, P. Julia, A. Tedgui, P. Codogno, C. M. Boulanger, P.-E. Rautou, Autophagy is required for endothelial cell alignment and atheroprotection under physiological blood flow. *Proc. Natl. Acad. Sci. U.S.A.* **114**, E8675–E8684 (2017).
9. D. Gibbings, S. Mostowy, F. Jay, Y. Schwab, P. Cossart, O. Voinnet, Selective autophagy degrades DICER and AGO2 and regulates miRNA activity. *Nat. Cell Biol.* **14**, 1314–1321 (2012).
10. P. N. Hsieh, G. Zhou, Y. Yuan, R. Zhang, D. A. Prosdocimo, P. Sangwung, A. H. Borton, E. Boriushkin, A. Hamik, H. Fujioka, C. E. Fealy, J. P. Kirwan, M. Peters, Y. Lu, X. Liao, D. Ramírez-Bergeron, Z. Feng, M. K. Jain, A conserved KLF-autophagy pathway modulates nematode lifespan and mammalian age-associated vascular dysfunction. *Nat. Commun.* **8**, 914 (2017).
11. S. H. Lan, S. Y. Wu, R. Zuchini, X. Z. Lin, I. J. Su, T. F. Tsai, Y. J. Lin, C. T. Wu, H. S. Liu, Autophagy suppresses tumorigenesis of hepatitis B virus-associated hepatocellular carcinoma through degradation of microRNA-224. *Hepatology* **59**, 505–517 (2014).
12. D. R. Sweet, L. Fan, P. N. Hsieh, M. K. Jain, Krüppel-like factors in vascular inflammation: Mechanistic insights and therapeutic potential. *Front. Cardiovasc Med.* **5**, 6 (2018).
13. A. Doddaballapur, K. M. Michalik, Y. Manavski, T. Lucas, R. H. Houtkooper, X. You, W. Chen, A. M. Zeiher, M. Potente, S. Dimmeler, R. A. Boon, Laminar shear stress inhibits endothelial cell metabolism via KLF2-mediated repression of PFKFB3. *Arterioscler. Thromb. Vasc. Biol.* **35**, 137–145 (2015).
14. S. Nicoli, C. Standley, P. Walker, A. Hurlstone, K. E. Fogarty, N. D. Lawson, MicroRNA-mediated integration of haemodynamics and Vegf signalling during angiogenesis. *Nature* **464**, 1196–1200 (2010).
15. K. M. Parmar, B. H. Larman, G. Dai, Y. Zhang, E. T. Wang, N. Moorthy, J. R. Kratz, Z. Lin, M. K. Jain, M. A. Gimbrone, Jr., G. García-Cardeña, Integration of flow-dependent endothelial phenotypes by Kruppel-like factor 2. *J. Clin. Invest.* **116**, 49–58 (2006).
16. A. Schober, M. Nazari-Jahantigh, Y. Wei, K. Bidzhekov, F. Gremse, J. Grommes, R. T. A. Megens, K. Heyll, H. Noels, M. Hristov, S. Wang, F. Kiessling, E. N. Olson, C. Weber, MicroRNA-126-5p promotes endothelial proliferation and limits atherosclerosis by suppressing Dlk1. *Nat. Med.* **20**, 368–376 (2014).
17. A. Schober, M. Nazari-Jahantigh, C. Weber, MicroRNA-mediated mechanisms of the cellular stress response in atherosclerosis. *Nat. Rev. Cardiol.* **12**, 361–374 (2015).
18. T. Thum, G. Condorelli, Long noncoding RNAs and MicroRNAs in cardiovascular pathophysiology. *Circ. Res.* **116**, 751–762 (2015).
19. A. Zernecke, K. Bidzhekov, H. Noels, E. Shagdarsuren, L. Gan, B. Denecke, M. Hristov, T. Köppel, M. Jahantigh, E. Lutgens, S. Wang, E. N. Olson, A. Schober, C. Weber, Delivery of microRNA-126 by apoptotic bodies induces CXCL12-dependent vascular protection. *Sci. Signal.* **2**, ra81 (2009).
20. J. E. Fish, M. Santoro, S. U. Morton, S. Yu, R.-F. Yeh, J. D. Wythe, K. N. Ivey, B. G. Bruneau, D. Y. R. Stainier, D. Srivastava, miR-126 regulates angiogenic signaling and vascular integrity. *Dev. Cell* **15**, 272–284 (2008).
21. T. A. Harris, M. Yamakuchi, M. Ferlito, J. T. Mendell, C. J. Lowenstein, MicroRNA-126 regulates endothelial expression of vascular cell adhesion molecule 1. *Proc. Natl. Acad. Sci. U.S.A.* **105**, 1516–1521 (2008).
22. S. Wang, A. B. Aurora, B. A. Johnson, X. Qi, J. McAnally, J. A. Hill, J. A. Richardson, R. Bassel-Duby, E. N. Olson, The endothelial-specific MicroRNA miR-126 governs vascular integrity and angiogenesis. *Dev. Cell* **15**, 261–271 (2008).
23. P. Hartmann, Z. Zhou, L. Natarelli, Y. Wei, M. Nazari-Jahantigh, M. Zhu, J. Grommes, S. Steffens, C. Weber, A. Schober, Endothelial Dicer promotes atherosclerosis and vascular inflammation by miRNA-103-mediated suppression of KLF4. *Nat. Commun.* **7**, 10521 (2016).
24. N. Baeyens, S. Nicoli, B. G. Coon, T. D. Ross, K. V. den Dries, J. Han, H. M. Lauridsen, C. O. Mejean, A. Eichmann, J.-L. Thomas, J. D. Humphrey, M. A. Schwartz, Vascular remodeling is governed by a VEGFR3-dependent fluid shear stress set point. *eLife* **4**, e04645 (2015).
25. S. Pitchiaya, L. A. Heinicke, J. I. Park, E. L. Cameron, N. G. Walter, Resolving subcellular miRNA trafficking and turnover at single-molecule resolution. *Cell Rep.* **19**, 630–642 (2017).
26. X. Yang, W. W. Du, H. Li, F. Liu, A. Khorshidi, Z. J. Rutnam, B. B. Yang, Both mature miR-17-5p and passenger strand miR-17-3p target TIMP3 and induce prostate tumor growth and invasion. *Nucleic Acids Res.* **41**, 9688–9704 (2013).
27. H.-W. Hwang, E. A. Wentzel, J. T. Mendell, A hexanucleotide element directs microRNA nuclear import. *Science* **315**, 97–100 (2007).
28. M. Benhamed, U. Herbig, T. Ye, A. Dejean, O. Bischof, Senescence is an endogenous trigger for microRNA-directed transcriptional gene silencing in human cells. *Nat. Cell Biol.* **14**, 266–275 (2012).
29. N. Martinez-Lopez, D. Athonvarangkul, P. Mishall, S. Sahu, R. Singh, Autophagy proteins regulate ERK phosphorylation. *Nat. Commun.* **4**, 2799 (2013).
30. Y. Kim, A. Maizel, X. Chen, Traffic into silence: Endomembranes and post-transcriptional RNA silencing. *EMBO J.* **33**, 968–980 (2014).
31. T. Ohrt, J. Mütze, W. Staroske, L. Weinmann, J. Höck, K. Crell, G. Meister, P. Schwille, Fluorescence correlation spectroscopy and fluorescence cross-correlation spectroscopy reveal the cytoplasmic origination of loaded nuclear RISC *in vivo* in human cells. *Nucleic Acids Res.* **36**, 6439–6449 (2008).
32. K. Nishi, A. Nishi, T. Nagasawa, K. Ui-Tei, Human TNRC6A is an Argonaute-navigator protein for microRNA-mediated gene silencing in the nucleus. *RNA* **19**, 17–35 (2013).
33. D. Schraivogel, G. Meister, Import routes and nuclear functions of Argonaute and other small RNA-silencing proteins. *Trends Biochem. Sci.* **39**, 420–431 (2014).
34. L. Weinmann, J. Höck, T. Ivacevic, T. Ohrt, J. Mütze, P. Schwille, E. Kremmer, V. Benes, H. Urlaub, G. Meister, Importin 8 is a gene silencing factor that targets argonaute proteins to distinct mRNAs. *Cell* **136**, 496–507 (2009).
35. K. Buchet-Poyau, J. Courchet, H. Hir, B. Séraphin, J.-Y. Scoazec, L. Duret, C. Domon-Dell, J.-N. Freund, M. Billaud, Identification and characterization of human Mex-3 proteins, a novel family of evolutionarily conserved RNA-binding proteins differentially localized to processing bodies. *Nucleic Acids Res.* **35**, 1289–1300 (2007).
36. B. Pereira, M. Borgne Le, N. T. Chartier, M. Billaud, R. Almeida, MEX-3 proteins: Recent insights on novel post-transcriptional regulators. *Trends Biochem. Sci.* **38**, 477–479 (2013).
37. L. Yang, C. Wang, F. Li, J. Zhang, A. Nayab, J. Wu, Y. Shi, Q. Gong, The human RNA-binding protein and E3 ligase MEX-3C binds the MEX-3–recognition element (MRE) motif with high affinity. *J. Biol. Chem.* **292**, 16221–16234 (2017).
38. T. C. Roberts, The microRNA biology of the mammalian nucleus. *Mol. Ther. Nucleic Acids* **3**, e188 (2014).

39. S. Kamada, U. Kikkawa, Y. Tsujimoto, T. Hunter, Nuclear translocation of caspase-3 is dependent on its proteolytic activation and recognition of a substrate-like protein(s). *J. Biol. Chem.* **280**, 857–860 (2005).
40. S. H. MacKenzie, C. A. Clark, Death by caspase dimerization. *Adv. Exp. Med. Biol.* **747**, 55–73 (2012).
41. K. Torisu, K. K. Singh, T. Torisu, F. Lovren, J. Liu, Y. Pan, A. Quan, A. Ramadan, M. Al-Omran, N. Pankova, S. R. Boyd, S. Verma, T. Finkel, Intact endothelial autophagy is required to maintain vascular lipid homeostasis. *Aging Cell* **15**, 187–191 (2016).
42. D. Sprott, D. M. Poitz, I. Korovina, A. Ziogas, J. Phieler, A. Chatzigeorgiou, I. Mitroulis, A. Deussen, T. Chavakis, A. Ameln, Endothelial-specific deficiency of ATG5 (autophagy protein 5) attenuates ischemia-related angiogenesis. *Arterioscler. Thromb. Vasc. Biol.* **39**, 1137–1148 (2019).
43. O. Tricot, Z. Mallat, C. Heymes, J. Belmin, G. Lesèche, A. Tedgui, Relation between endothelial cell apoptosis and blood flow direction in human atherosclerotic plaques. *Circulation* **101**, 2450–2453 (2000).
44. F. M. Barriga, E. Montagni, M. Mana, M. Mendez-Lago, X. Hernando-Momblona, M. Sevillano, A. Guillaumet-Adkins, G. Rodriguez-Esteban, S. J. A. Buczacki, M. Gut, H. Heyn, D. J. Winton, O. H. Yilmaz, C. S. Attolini, I. Gut, E. Batlle, Mex3a marks a slowly dividing subpopulation of Lgr5+ intestinal stem cells. *Cell Stem Cell* **20**, 801–816.e7 (2017).
45. E. Elkayam, C.-D. Kuhn, A. Tocilj, A. D. Haase, E. M. Greene, G. J. Hannon, L. Joshua-Tor, The structure of human argonaute-2 in complex with miR-20a. *Cell* **150**, 100–110 (2012).
46. N. T. Schirle, J. Sheu-Gruttadauria, I. J. MacRae, Structural basis for microRNA targeting. *Science* **346**, 608–613 (2014).
47. P. Wild, D. G. McEwan, I. Dikic, The LC3 interactome at a glance. *J. Cell Sci.* **127**, 3–9 (2014).
48. G. Mariño, M. Niso-Santano, E. H. Baehrecke, G. Kroemer, Self-consumption: The interplay of autophagy and apoptosis. *Nat. Rev. Mol. Cell Bio.* **15**, 81–94 (2014).
49. S. Nagata, Apoptosis and clearance of apoptotic cells. *Annu. Rev. Immunol.* **36**, 489–517 (2018).
50. A. Belter, D. Gudanis, K. Rolle, M. Piwecka, Z. Gdaniec, M. Z. Naskręt-Barciszewska, J. Barciszewski, Mature miRNAs form secondary structure, which suggests their function beyond RISC. *PLOS ONE* **9**, e113848 (2014).
51. R. Horos, M. Büscher, R. Kleinendorst, A.-M. Alleaume, A. K. Tarafder, T. Schwarzl, D. Dziuba, C. Tischer, E. M. Zielonka, A. Adak, A. Castello, W. Huber, C. Sachse, M. W. Hentze, The small non-coding vault RNA1-1 acts as a riboregulator of autophagy. *Cell* **176**, 1054–1067.e12 (2019).
52. D. de Rie, I. Abugessaisa, T. Alam, E. Arner, P. Arner, H. Ashoor, G. Åström, M. Babina, N. Bertin, A., M. Burroughs, A. J. Carlisle, C. O. Daub, M. Detmar, R. Deviatiiarov, A. Fort, C. Gebhard, D. Goldowitz, S. Guhl, T. J. Ha, J. Harshbarger, A. Hasegawa, K. Hashimoto, M. Herlyn, P. Heutink, K. J. Hitchens, C. C. Hon, E. Huang, Y. Ishizu, C. Kai, T. Kasukawa, P. Klinken, T. Lassmann, C.-H. Lecellier, W. Lee, M. Lizio, V. Makeev, A. Mathelier, Y. A. Medvedeva, N. Mejhert, C. J. Mungall, S. Noma, M. Ohshima, M. Okada-Hatakeyama, H. Persson, P. Rizzu, F. Roudnicky, P. Sætrom, H. Sato, J. Severin, J. W. Shin, R. K. Swoboda, H. Tarui, H. Toyoda, K. Vitting-Seerup, L. Winteringham, Y. Yamaguchi, K. Yasuzawa, M. Yoneda, N. Yumoto, S. Zabierowski, P. G. Zhang, C. A. Wells, K. M. Summers, H. Kawaji, A. Sandelin, M. Rehli, T. Consortium; FANTOM, Y. Hayashizaki, P. Carninci, A. R. R. Forrest, M. J. L. de Hoon, An integrated expression atlas of miRNAs and their promoters in human and mouse. *Nat. Biotechnol.* **35**, 872–878 (2017).
53. A. Barilli, R. Visigalli, R. Sala, G. C. Gazzola, A. Parolari, E. Tremoli, S. Bonomini, A. Simon, E. I. Closs, V. Dall'Asta, O. Bussolati, In human endothelial cells rapamycin causes mTORC2 inhibition and impairs cell viability and function. *Cardiovasc. Res.* **78**, 563–571 (2008).
54. A.-C. Vion, B. Ramkhelawon, X. Loyer, G. Chironi, C. Devue, G. Loirand, A. Tedgui, S. Lehoux, C. M. Boulanger, Shear stress regulates endothelial microparticle release. *Circ. Res.* **112**, 1323–1333 (2013).
55. M. W. Hentze, A. Castello, T. Schwarzl, T. Preiss, A brave new world of RNA-binding proteins. *Nat. Rev. Mol. Cell Bio.* **19**, 327–341 (2018).
56. A. M. Choi, S. W. Ryter, B. Levine, Autophagy in human health and disease. *N. Engl. J. Med.* **368**, 651–662 (2013).
57. P. Carmeliet, Angiogenesis in life, disease and medicine. *Nature* **438**, 932–936 (2005).
58. Y. Yan, D. Zhang, P. Zhou, B. Li, S.-Y. Huang, HDOCK: A web server for protein–protein and protein–DNA/RNA docking based on a hybrid strategy. *Nucleic Acids Res.* **45**, W365–W373 (2017).
59. G. C. P. van Zundert, J. P. G. L. M. Rodrigues, M. Trellet, C. Schmitz, P. L. Kastritis, E. Karaca, A. S. J. Melquiond, M. van Dijk, S. J. de Vries, A. M. J. J. Bonvin, The HADDOCK2.2 web server: User-friendly integrative modeling of biomolecular complexes. *J. Mol. Biol.* **428**, 720–725 (2016).
60. P. von Hundelshausen, S. M. Agten, V. Eckardt, X. Blanchet, M. M. Schmitt, H. Ippel, C. Neideck, K. Bidzhekov, J. Leberzammer, K. Wichapong, A. Faussner, M. Drechsler, J. Grommes, J. P. van Geffen, H. Li, A. Ortega-Gomez, R. T. Megens, R. Naumann, I. Dijkgraaf, G. A. Nicolaes, Y. Döring, O. Soehnlein, E. Lutgens, J. W. Heemskerk, R. R. Koenen, K. H. Mayo, T. M. Hackeng, C. Weber, Chemokine interactome mapping enables tailored intervention in acute and chronic inflammation. *Sci. Transl. Med.* **9**, eaah6650 (2017).
61. K. Wichapong, J.-E. Alard, A. Ortega-Gomez, C. Weber, T. M. Hackeng, O. Soehnlein, G. A. F. Nicolaes, Structure-based design of peptidic inhibitors of the interaction between CC chemokine ligand 5 (CCL5) and human neutrophil peptides 1 (HNP1). *J. Med. Chem.* **59**, 4289–4301 (2016).
62. P. V. Konarev, V. V. Volkov, A. V. Sokolova, M. H. J. Koch, D. I. Svergun, *PRIMUS*: A windows PC-based system for small-angle scattering data analysis. *J. Appl. Cryst.* **36**, 1277–1282 (2003).
63. M. V. Petoukhov, D. Franke, A. V. Shkumatov, G. Tria, A. G. Kikhney, M. Gajda, C. Gorba, H. D. T. Mertens, P. V. Konarev, D. I. Svergun, New developments in the *ATSAS* program package for small-angle scattering data analysis. *J. Appl. Crystallogr.* **45**, 342–350 (2012).
64. F. Delaglio, S. Grzesiek, G. W. Vuister, G. Zhu, J. Pfeifer, A. Bax, NMRPipe: A multidimensional spectral processing system based on UNIX pipes. *J. Biomol. NMR* **6**, 277–293 (1995).
65. B. A. Johnson, R. A. Blevins, NMR View: A computer program for the visualization and analysis of NMR data. *J. Biomol. NMR* **4**, 603–614 (1994).
66. S. Giebe, N. Cockcroft, K. Hewitt, M. Brux, A. Hofmann, H. Morawietz, C. Brunssen, Cigarette smoke extract counteracts atheroprotective effects of high laminar flow on endothelial function. *Redox Biol.* **12**, 776–786 (2017).
67. C. Brunssen, S. Korten, M. Brux, S. Seifert, J. Roesler, S. R. Bornstein, H. Morawietz, W. Goettsch, COUP-TFII is regulated by high glucose in endothelial cells. *Horm. Metab. Res.* **42**, 81–87 (2010).
68. C. Mahl, V. Egea, R. T. Megens, T. Pitsch, D. Santovito, C. Weber, C. Ries, RECK (reversion-inducing cysteine-rich protein with Kazal motifs) regulates migration, differentiation and Wnt/β-catenin signaling in human mesenchymal stem cells. *Cell. Mol. Life Sci.* **73**, 1489–1501 (2016).
69. M. W. Pfaffl, G. W. Horgan, L. Dempfle, Relative expression software tool (REST©) for group-wise comparison and statistical analysis of relative expression results in real-time PCR. *Nucleic Acids Res.* **30**, e36 (2002).
70. J. Schindelin, I. Arganda-Carreras, E. Frise, V. Kaynig, M. Longair, T. Pietzsch, S. Preibisch, C. Rueden, S. Saalfeld, B. Schmid, J.-Y. Tinevez, D. White, V. Hartenstein, K. Eliceiri, P. Tomancak, A. Cardona, Fiji: An open-source platform for biological-image analysis. *Nat. Methods* **9**, 676–682 (2012).
71. L. Natarelli, C. Geißler, G. Csaba, Y. Wei, M. Zhu, A. di Francesco, P. Hartmann, R. Zimmer, A. Schober, miR-103 promotes endothelial maladaptation by targeting lncWDR59. *Nat. Commun.* **9**, 2645 (2018).
72. D. W. Huang, B. T. Sherman, R. A. Lempicki, Systematic and integrative analysis of large gene lists using DAVID bioinformatics resources. *Nat. Protoc.* **4**, 44–57 (2009).
73. M. Krzywinski, J. Schein, İ. Birol, J. Connors, R. Gascoyne, D. Horsman, S. J. Jones, M. A. Marra, Circos: An information aesthetic for comparative genomics. *Genome Res.* **19**, 1639–1645 (2009).
74. C. A. Klattenhoff, J. C. Scheuermann, L. E. Surface, R. K. Bradley, P. A. Fields, M. L. Steinhauser, H. Ding, V. L. Butty, L. Torrey, S. Haas, R. Abo, M. Tabebordbar, R. T. Lee, C. B. Burge, L. A. Boyer, *Braveheart*, a long noncoding RNA required for cardiovascular lineage commitment. *Cell* **152**, 570–583 (2013).
75. M. Popenda, M. Szachniuk, M. Antczak, K. J. Purzycka, P. Lukasiak, N. Bartol, J. Blazewicz, R. W. Adamiak, Automated 3D structure composition for large RNAs. *Nucleic Acids Res.* **40**, e112 (2012).
76. C. Pop, Y.-R. Chen, B. Smith, K. Bose, B. Bobay, A. Tripathy, S. Franzen, A. C. Clark, Removal of the pro-domain does not affect the conformation of the procaspase-3 dimer. *Biochemistry* **40**, 14224–14235 (2001).
77. J. Pfaff, J. Hennig, F. Herzog, R. Aebersold, M. Sattler, D. Niessing, G. Meister, Structural features of Argonaute–GW182 protein interactions. *Proc. Natl. Acad. Sci. U.S.A.* **110**, E3770–E3779 (2013).
78. J. Füllgrabe, G. Ghislat, D.-H. Cho, D. C. Rubinsztein, Transcriptional regulation of mammalian autophagy at a glance. *J. Cell Sci.* **129**, 3059–3066 (2016).

Acknowledgments: We thank M. Haberbosch, T. Pitsch, and D. Wagner for technical assistance, A. di Francesco for experimental help with in situ PCR, and R. Boon (University of Frankfurt) for providing RNA from Cdh5^{Cre}Klf2$^{fl/fl}$ mice. We thank R. Stehle and the SAXS facility of the SFB1035 at the Department of Chemistry, Technical University of Munich and G. Meister (University of Regensburg) for sharing the Ago2 plasmid and for helpful discussion. pET21b-caspase-3 was a gift from C. Clark. D.S. thanks A. Consoli for support during doctoral studies. C.W. is a Van de Laar professor of atherosclerosis. **Funding:** This work was supported by Deutsche Forschungsgemeinschaft (DFG), TRR267-A2 to C.W. and M.S., INST409/150-1 FUGG to R.T.A.M. and C.W., SFB1123-A1/10/B4 to C.W. and J.D., SFB1123-A2 to P.v.H., SFB1123-Z1 to R.T.A.M., SFB1123-A5 to E.L., STE-1053/5-1 to S.S., SFB1035 and GRK1721 to M.S., by the Italian Ministry of University and Research and the Italian Society of Internal Medicine (premi di ricerca 2013) to D.S., and by the European Research Council (ERC AdG 692511 to C.W. and ERC CoG 683145 to T.C.). **Author contributions:** D.S. designed and

performed experiments, analyzed data, and wrote the manuscript. V.E., K.B., L.N., A.M., and R.T.A.M. designed and performed experiments, analyzed data, and contributed to writing the manuscript. X.B., K.W., M.A., C.B., M. Horckmans, M. Hristov and A.G. performed experiments and analyzed data. E.L. and M.J.A.P.D. provided human plaque material and analysis. T.H., C.R., P.v.H., H.M., and S.S. analyzed data and provided funding and supervision. T.C. provided critical reagents and intellectual input. R.N. critically contributed to mouse transgenesis. J.D. and M.S. analyzed data, provided supervision and intellectual input, and contributed to writing the manuscript. C.W. conceived and supervised the study, designed experiments, provided funding, and wrote the manuscript. **Competing interests:** The authors declare that they have no competing interests. **Data and materials availability:** All data associated with this study are present in the main text or the Supplementary Materials.

Submitted 22 August 2019
Accepted 2 April 2020
Published 3 June 2020
10.1126/scitranslmed.aaz2294

Citation: D. Santovito, V. Egea, K. Bidzhekov, L. Natarelli, A. Mourão, X. Blanchet, K. Wichapong, M. Aslani, C. Brunßen, M. Horckmans, M. Hristov, A. Geerlof, E. Lutgens, M. J. A. P. Daemen, T. Hackeng, C. Ries, T. Chavakis, H. Morawietz, R. Naumann, P. von Hundelshausen, S. Steffens, J. Duchêne, R. T. A. Megens, M. Sattler, C. Weber, Noncanonical inhibition of caspase-3 by a nuclear microRNA confers endothelial protection by autophagy in atherosclerosis. *Sci. Transl. Med.* **12**, eaaz2294 (2020).

Science Translational Medicine

Noncanonical inhibition of caspase-3 by a nuclear microRNA confers endothelial protection by autophagy in atherosclerosis

Donato Santovito, Virginia Egea, Kiril Bidzhekov, Lucia Natarelli, André Mourão, Xavier Blanchet, Kanin Wichapong, Maria Aslani, Coy Brunßen, Michael Horckmans, Michael Hristov, Arie Geerlof, Esther Lutgens, Mat J.A.P. Daemen, Tilman Hackeng, Christian Ries, Triantafyllos Chavakis, Henning Morawietz, Ronald Naumann, Philipp von Hundelshausen, Sabine Steffens, Johan Duchêne, Remco T.A. Megens, Michael Sattler and Christian Weber

Sci Transl Med **12**, eaaz2294.
DOI: 10.1126/scitranslmed.aaz2294

Autophagy and atherosclerosis

Autophagy is one mechanism by which cells adapt to stress. Here, Santovito *et al.* investigated the role of microRNA (miR) 126-5p in endothelial cell autophagy in atherosclerosis. The authors observed that high shear stress promoted trafficking of miR-126-5p to the nucleus of endothelial cells where it had antiapoptotic effects via direct interaction with caspase-3. This pathway was present in the aortas of mouse models of atherosclerosis and samples of diseased vessels from humans. Results uncover a noncanonical mechanism by which miR-126-5p prevents endothelial dysfunction.